Esha Mishra, Subrata Majumder, Shikha Varma\* and Peter A. Dowben

# X-ray photoemission studies of the interaction of metals and metal ions with DNA

https://doi.org/10.1515/zpch-2021-3037 Received March 8, 2021; accepted October 28, 2021; published online November 16, 2021

**Abstract:** X-ray Photoelectron Spectroscopy (XPS) has been used to study the interactions of heavy metal ions with DNA with some success. Surface sensitivity and selectivity of XPS are advantageous for identifying and characterizing the chemical and elemental structure of the DNA to metal interaction. This review summarizes the status of what amounts to a large part of the photoemission investigations of biomolecule interactions with metals and offers insight into the mechanism for heavy metal-bio interface interactions. Specifically, it is seen that metal interaction with DNA results in conformational changes in the DNA structure.

**Keywords:** DNA; DNA coordination chemistry; mercury; X-ray photoemission spectroscopy.

#### 1 Introduction

The interaction of metals with DNA is important as heavy metals are frequently toxic and a global public health issue. In particular, metals are known to have significant bio interactions and include the metals/metalloids such as chromium (Cr), copper (Cu), arsenic (As), cadmium (Cd), and silver (Ag) as well as the obvious heavy metals mercury (Hg) and lead (Pb) [1]. In addition, heavy metals have been

<sup>\*</sup>Corresponding author: Shikha Varma, Institute of Physics, Sachivalaya Marg, Bhubaneswar 751005, India; and Homi Bhabha National Institute, Training School Complex, Anushakti Nagar, Mumbai 400085, India, E-mail: shikha@iopb.res.in

Esha Mishra and Peter A. Dowben, Department of Physics and Astronomy, University of Nebraska–Lincoln, Jorgenson Hall, 855 North 16th Street, Lincoln, NE 68588-0299, USA Subrata Majumder, Department of Physics, National Institute of Technology, Patna, Bihar 800005, India

reported to affect the biological system by disturbing biological processes such as metabolism, damage repair, and detoxification [2]. Depending upon the physical and chemical properties, the formation of reactive species by the process of autoxidation, the blockage of some functional group by the metal ions in the biomolecules, and displacement of specific metal ions from the biomolecules are the three major mechanisms by which the heavy metal ions affect the biological system [3, 4].

Much of the X-ray photoemission investigations of heavy metal interactions with biomolecules have centered on DNA. There are two general categories of interactions of DNA with heavy metal ions. First, the interaction between the metal ions and DNA can lead to strand breaks in the DNA, as shown in Figure 1 [5]. Secondly, there are DNA molecules, called DNAzymes, which are catalytically active and use metal cofactors for the purpose of enzymatic functions [6]. The sensors with these catalytic DNA are reported to have higher selectivity towards specific metal ions [7]. Due to its sensitivity and selectivity, even in the complex environment, DNAzymes based biosensors are insensitive towards other atoms and metal ions present in the biomolecules [8–10]. Barlow et al. [11] discussed the preferential binding nature of amino acids towards a specific metal surface. Studies conducted by Marti et al. [12] demonstrated that the bond was formed by

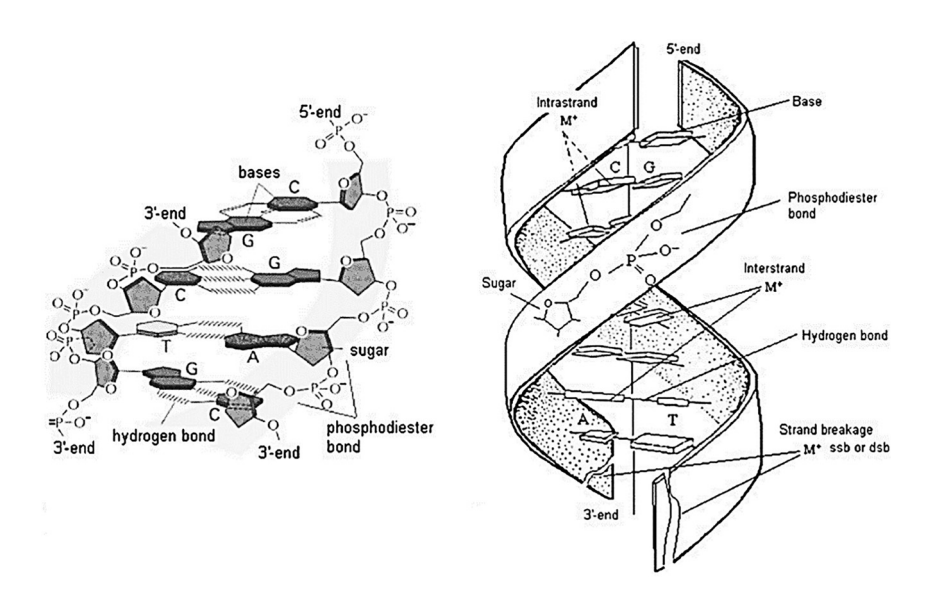


**Figure 1:** Double helix structure of DNA with hydrogen bonds, phosphodiester bond [left], to illustrate that the binding of metal ions can occur to either interstrand or intrastrand of the double-stranded DNA [right] [5].

the carboxylate group of histidine on the gold surface and by the amino group of histidine on the copper surface. The study of the interaction of peptides with the metal oxides is critical because peptides can bind to inorganic surfaces as hetero linkers leading to the formation and development of controlled assemblies of nanoparticles [13].

Surface studies of biological systems are very challenging because, i) molecules based on organocarbon can be damaged by the surface probes, ii) biological molecules are highly complex in comparison to any other inorganic or organic system, iii) surface analysis is done in ultrahigh vacuum (UHV) system which is a very different environment compared to the normal aqueous media typical of biological systems, and iv) the irregular shape of biological surface specimens [14]. While the very valuable results of photoemission studies of heavy metal interactions with the various biomolecules must be interpreted cautiously. Yet the photoemission studies, nonetheless, aid in understanding the influence of a physical environment on the biological system [15]. The XPS core level binding energies are characteristic of not only a particular element but can be used for the identification and characterization of the chemical shifts that result from changes in the chemical bonding environment [16]. The photoemission is final state spectroscopy, and the measured core level binding energy is not only influenced by the change in the electronic charge density of both the initial and the final states. The core level binding energy shift has a direct dependence on the change in electronic charge densities and can also be perturbed towards higher binding energies in the case of dielectric or nonmetallic systems [17].

Despite the many complications, X-ray photoemission spectroscopy (XPS) has been widely used to detect the presence of contaminants such as hydrocarbons, silicones, or any other chemical substances that might disturb the biological function in a system [15]. The surface sensitivity and selectivity of the XPS technique helps in choosing an appropriate material for bioengineering purposes based on their optical or mechanical properties [15]. The surface sensitivity of XPS with regard to determining the composition of materials can be explained via relatively short inelastic mean free path (IMPF), the IMPF being the average of distance traveled by the electrons between the successive inelastic collisions [18]. The probing depth of XPS is limited as the escape depth photoelectrons travel is a few nanometers or less below the surface, and thus provides valuable information regarding the surface region [19]. The XPS analysis was used to study the changes in the oxidation states of chromium in aerobic and anaerobic Shewanella oneidensis cells [20]. The chemical composition at the surface of nine different Bacillus subtilis strains were also studied using XPS analysis [21]. Angle-resolved XPS was used to study the compatibility of blood with PVCs (pure polyvinyl chloride) and on PVC-b (polyvinyl chloride from a blood bag) [22]. Surface oxide films on the 316L stainless steel placed in different environments were characterized using XPS to estimate the construction of biocompatible films in the human body [23]. Even in recent years, there have been notable number of studies utilizing the XPS technique as one of the tools to explore the interaction of DNA with different forms of metals [24–26]. This review seeks to illustrate the value in using X-ray photoemission spectroscopic methods to obtain insights into the mechanisms involved in heavy metals-bio interface interactions.

## 2 XPS study of the interaction of nucleotide bases with metals

The nucleotide bases adenine (A), cytosine (C), guanine (G), and thymine (T) are the basic constituents of DNA. While the nucleic acids are not DNA, XPS taken to investigate how nucleotide bases interact with metals does provide some essential reference XPS spectra. There has been a significant amount of effort, using XPS, to understand the interaction of these nucleotide bases with some metal surfaces [27–29]. Tsud et al. [30] investigated the adsorption of adenine adlayers on Cu(111) using adenine coverages of 1.6 and 0.4 molecular monolayers (ML) [30]. The adenine adlayers were initially deposited on the Cu(111) at 25 °C via the evaporation, and then the XPS measurements were carried out after annealing at different temperatures [30].

Figure 2 (a and b) and Figure 2 (c and d) shows the core level C 1s, N 1s XPS spectra for 1.6 monolayers (ML) and 0.4 ML adenine coverage on Cu(111), respectively. The C 1s core-level spectra in both the cases for the initial deposition of adenine on Cu(111) shows three distinct components A, B, and C, where component A is the representative of the C6 carbon, component B represents C2, C4, C8 carbons and component C represents C5 carbon of the adenine molecule [31, 32]. In the case of 1.6 ML adenine, 0.4 eV shift of C 1s spectra towards the lower binding energy at the annealing temperature of 75 and 100 °C is observed, indicating the effect of core hole screening in the case of lower adenine coverage. If we compare the photoemission C 1s core level spectra of both cases, there is no significant change in the component A up to 125 °C for 1.6 ML adenine and up to 100 °C for 0.4 ML adenine. However, a decrease in the intensity of component A of the C 1s core level spectra was observed at higher temperatures and since this component represents C6 carbon, it is expected that the bonding between Cu(111) substrate and the adenine changes, likely in the region of C6 carbon [30].

As shown in Figure 2 (b and d), in the case of N 1s spectra, initially after the deposition of adenine, the D and E components are prominently observed for both of the coverages of adenine on Cu(111). The D component was assigned to the

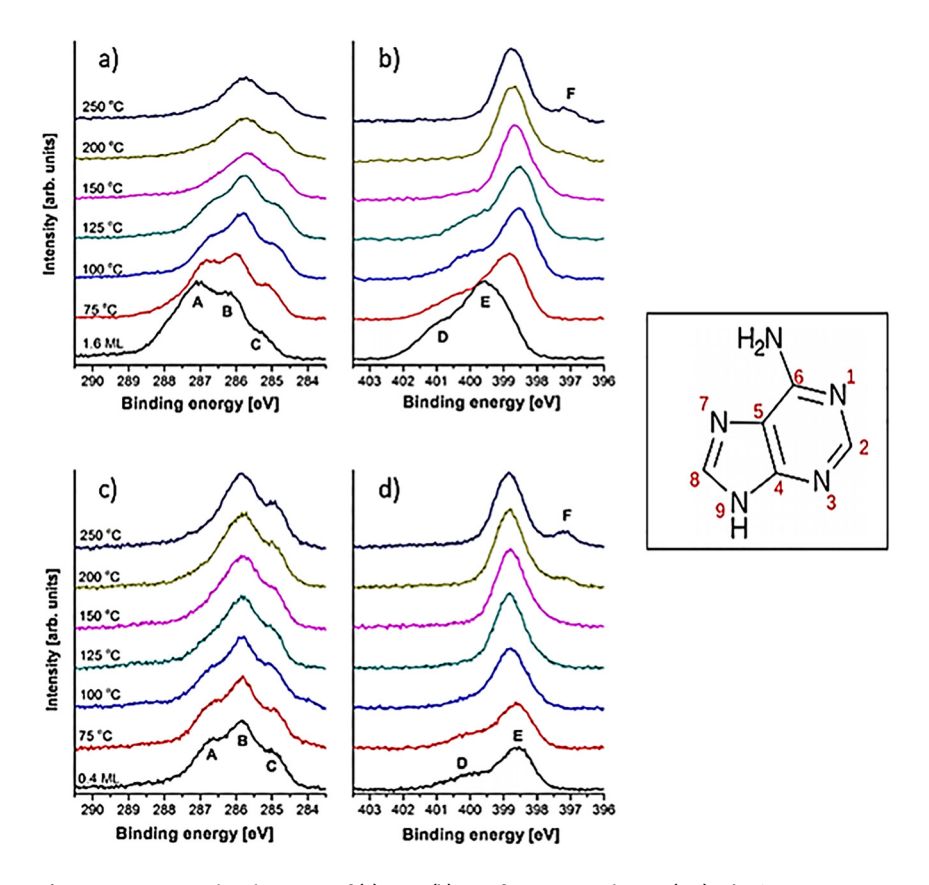


**Figure 2:** XPS core-level spectra of (a) C 1s, (b) N 1s for 1.6 monolayers (ML) adenine coverage on the Cu (111) and (c) C 1s, (d) N 1s for adenine coverage of 0.4 ML on Cu (111). Image on the right is the schematic representation of the nucleic acid adenine [30].

amino nitrogen whereas E component was assigned to the imino nitrogen [30]. However, after annealing at 100 °C, a decrease in intensity along with a 1.0 eV shift, towards smaller binding energies, was observed for 1.6 ML adenine on Cu(111). This N 1s core level binding energy shift indicates a significant change in the environment of the nitrogen atom and could include contributions from hydrogen bonding. The D component of the N 1s core level spectra was then attributed to N9 atom [33]. The E component becomes significant after annealing 1.6 ML adenine on Cu(111) to 125 °C and to 100 °C for 0.4 ML adenine on Cu(111). The nitrogen atoms in adenine have multiple bonding configurations, affecting the E component in the N 1s spectra including shifts in binding energy. After annealing at 200 °C, the presence of F component in the N 1s spectra at a binding energy of 397.0 eV was

attributed to the direct bonding of adenine N to the copper substrate [34]. The presence of bond between Cu(111) and adenine is confirmed by the 0.2 eV shift towards the higher binding energy of E component in the N 1s spectra with F component being absent [30]. Therefore, the XPS studies of the adenine layers on Cu substrate confirms the presence of bonding between the Cu substrate and adenine. This does really provide insight into how the two polynucleotide chains of DNA might interact with a metal like copper.

### 3 XPS study of phosphomolybdic acid (PMA)/ adenine or thymine/[AuCl<sub>4</sub>]<sup>-</sup> or [Ag]<sup>+</sup> nanostructures

The interaction of the phosphomolybdic acid (PMA) with the nucleobases adenine/thymine and silver/gold metal ions was utilized to construct composite nanostructures [35]. Six nanostructures were synthesized in this study, the synthesized composites being: i) PMA and adenine composite (PMA/A), ii) PMA, adenine and [AuCl<sub>4</sub>]<sup>-</sup> composite (PMA/A/Au), iii) PMA, adenine and [Ag]<sup>+</sup> composite (PMA/A/Ag), iv) PMA and thymine composite (PMA/T), v) PMA, thymine and [AuCl<sub>4</sub>]<sup>-</sup> composite (PMA/T/Au) and vi) PMA, thymine and [Ag]<sup>+</sup> composite (PMA/T/Ag). In addition, XPS was used to study the changes in the chemical states of the six different nanostructure composites during the process of self-assembly [35].

Figure 3 shows the N 1s, O 1s and C 1s core level XPS spectra for adenine (A), PMA/A, PMA/A/Ag, PMA/A/Au and thymine (T), PMA/T, PMA/T/Ag and PMA/T/Au as labelled. In XPS, two different chemical states of nitrogen are evident from N 1s core level components at binding energies of 400.3 and 398.8 eV corresponding to the amine group, and ring nitrogen respectively. The interaction of PMA with purine, via protonation, is indicated by the binding energy shift towards the higher values for aniline and purine nitrogen along with the binding energy shift towards the lower value for the imidazole ring. The shift of N 1s spectra towards the higher binding energy is observed for PMA/A/Au indicating a possible interaction of imidazole nitrogen and  $[AuCl_a]^-$  [35]. Since the  $[AuCl_a]^$ and [Ag]<sup>+</sup> in the composite nanostructures were present as anion and cation respectively, the positively charged [Ag]<sup>+</sup> cation forms a stronger bond with the PMA [36, 37] giving rise to an extra peak in the N 1s spectra of PMA/A/Ag. The appearance of three different nitrogen components at 397.9, 399.4 and 401.1 eV, in the N 1s XPS spectra, indicate the bonding of the PMA with the ring nitrogen. The O 1s core level spectra of the pure PMA shows two distinct peaks at 531.2 and 532.6 eV corresponding to two different chemical states. The shift of the O 1s core level peak at 531.2 eV towards the lower binding energy of 530.9 eV was observed for PMA/A, PMA deprotonation and the binding of protonated nucleobase with PMA being the main cause. No significant change in the spectral profile of O 1s was observed after the addition of the Au anion to PMA/A, however the addition of silver cations seemed to affect the O 1s peak profile significantly, indicating the interaction of silver cations with PMA and an interaction of  $[AuCl_4]^-$  anions with the nucleotide [35].

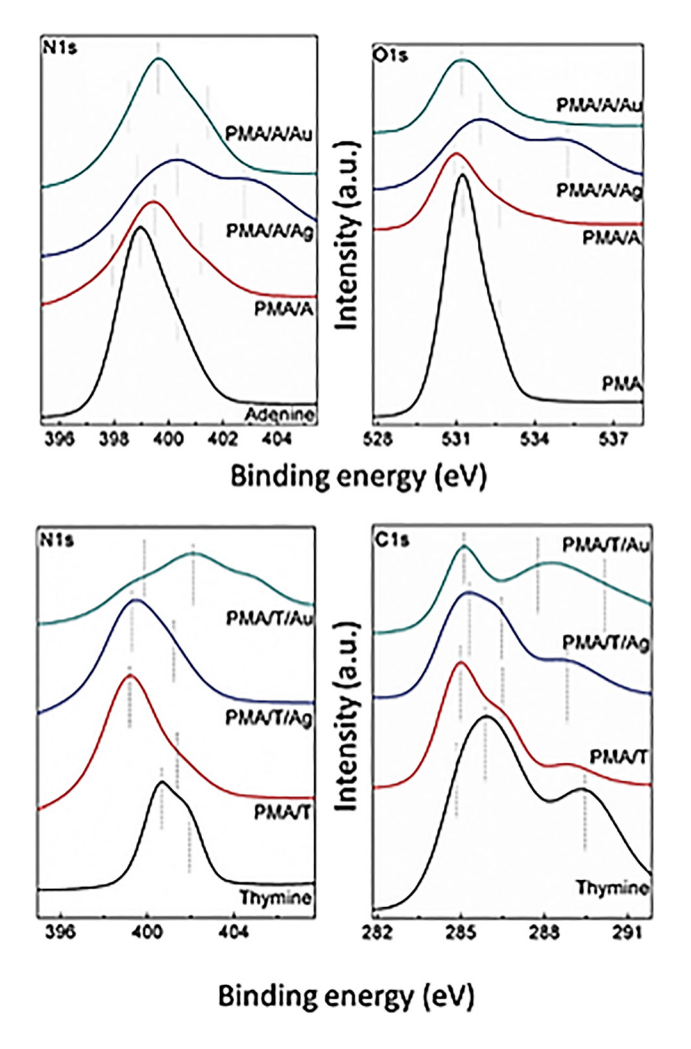
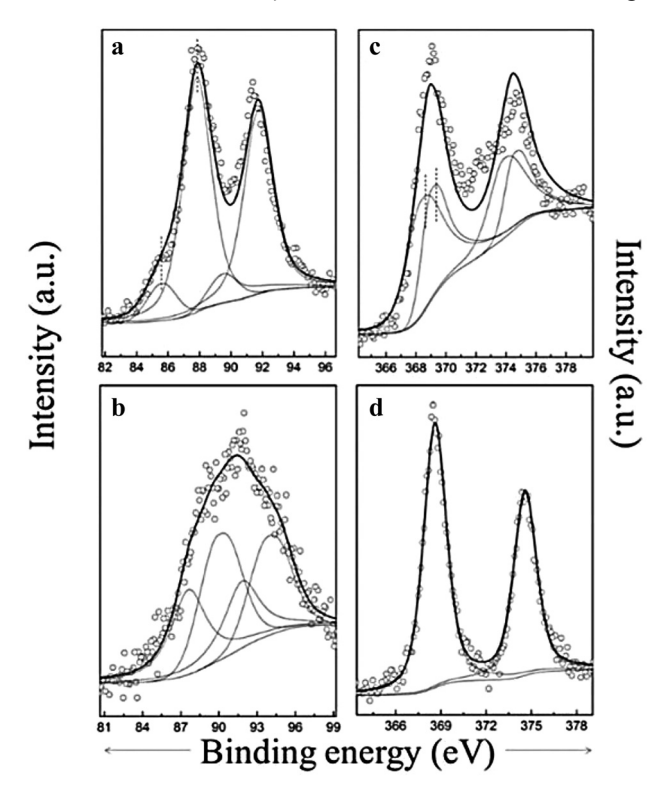


Figure 3: XPS N 1s, O 1s and C 1s core level spectra for adenine (A), PMA/A, PMA/A/Ag, PMA/A/Au and thymine (T), PMA/T, PMA/T/Ag and PMA/T/Au [35].

The XPS spectra of N 1s for thymine has two distinct chemical states at 400.6 and 401.9 eV corresponding to two distinct heterocyclic nitrogens in thymine. Adding thymine to PMA caused the N 1s peaks to shift towards the lower binding energies of 399.2 and 401.5 eV, as evident in the N 1s spectra of PMA/T. For PMA/T/Ag, there is no significant change in the peak profile, however, the peak profile changes for PMA/T/Au [35]. The C 1s XPS spectra indicates that there are two distinct chemical states for pure thymine, one at 286.3 eV corresponding to the carbon-nitrogen bond and the other at 289.4 eV corresponding to the carbon oxygen bond. For PMA/T, the C 1s spectral shift to a lower binding energy value of 288.8 eV, from 289.4 eV, is thought to indicate the carbonyl oxygen protonation [35].

The Au 4f XPS spectra of PMA/A/Au and PMA/T/Au complexes are presented in Figure 4 (a and b) respectively. For PMA/A/Au, in the Au 4f<sub>7/2</sub> components, the feature at 85.5 eV corresponds to Au(I) species, an indication of a complex formation between [AuCl<sub>4</sub>] and adenine because of the higher binding energy than



**Figure 4:** Au 4fXPS spectra of a) PMA/A/Au, b) PMA/T/Au and Ag 3d XPS spectra of c) PMA/A/Ag, d) PMA/T/Ag [35].

metallic gold (Au). For PMA/T/Au, the Au 4f peak did not exhibit a significant shift in binding energy, although a change in the Au 4f peak profile indicated weak interactions between the [AuCl<sub>4</sub>] and PMA/T [35]. The Ag 3d XPS spectra is shown in Figure 4 (c and d) for PMA/A/Ag and PMA/T/Ag respectively. The two Ag  $3d_{5/2}$  features at binding energies of 369 and 368.3 eV were observed for PMA/A/Ag, the 368.3 eV peak corresponding to the reduction of Ag<sup>+</sup> ions by the nucleobases into metallic silver [35]. For PMA/T/Ag, the peak at 368.6 eV is higher in comparison to metallic silver whereas lower in comparison to Ag<sup>+</sup> ions denoting the transfer of electrons between the Ag<sup>+</sup> ions and thymine [35]. These insights into the interaction of single nucleotides with silver is important as silver is a bioactive, and the interaction of the silver with DNA has been explored, as discussed later in this article.

# 4 Characterization of mercury ions nanosensor based on thymine functionalized Au nanoparticles

Thymine is considered as a very effective ligand for the binding of mercury ions [38]. Yuan et al. studied highly sensitive thymine-gold nanoparticles-based fiber optic surface plasmon resonance nanosensor for the detection of  $Hg^{2+}$  ions [39]. The Au coated optic fibers were functionalized using 2-aminoethanethiol (AET) which contains a thiol group that could form a strong bond with the Au surface. The reaction of the amide group of the Au nanoparticles/AET system with thymine-COOH, through the process of condensation, results into the formation of Au nanoparticles/thymine. XPS was used to characterize the process of functionalization in this system.

Figure 5 (a–c) shows the XPS core level spectra of N 1s, S 2p and O 1s respectively for Au nanoparticles/AET system. In Figure 5 (a), the N 1s peak at a binding energy of 399.4 eV was assigned to the N–C bonds of the AET adsorbed on the surface of Au-nanoparticles [39]. The occurrence of doublet peaks, most likely due to spin–orbit splitting in the S 2p spectra, in Figure 5 (b) indicates the presence of thiol group in the system. Since optical fibers were made up of silicon dioxide, the O 1s peak at 531.1 eV for Au nanoparticles/AET attributes to the Si–O bonding [39]. Likewise, Figure 5 (d–f) shows the XPS core level spectra of N 1s, S 2p and O 1s respectively for Au nanoparticles/thymine system. The two distinct peaks at binding energies of 399.2 and 400.9 eV in the N 1s core level spectra for Au nanoparticles/thymine were assigned to O=C–N and C–N respectively [39]. This also indicates the N–C bond formation is due to the condensation of NH<sub>2</sub> of the

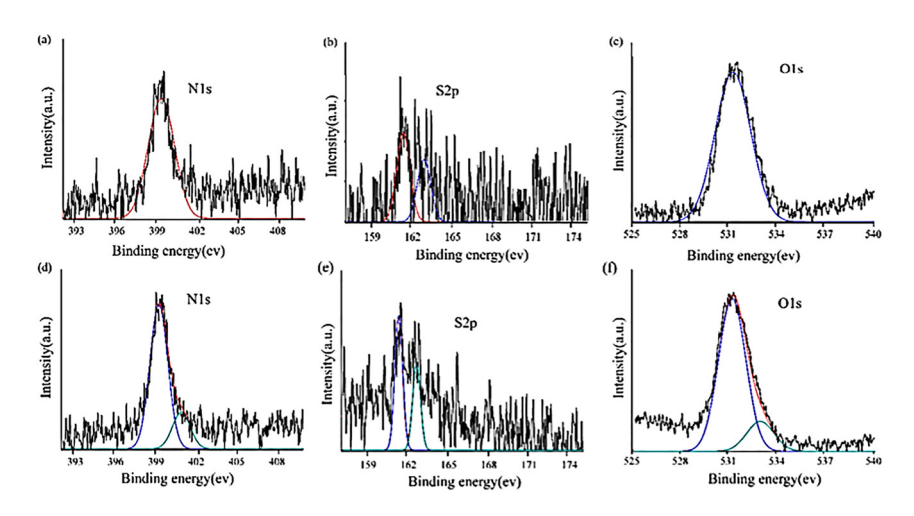


**Figure 5:** XPS core level spectra of (a) N 1s, (b) S 2p (c) O 1s for Au nanoparticles/AET system and (d) N 1s, (e) S 2p (f) O 1s for Au nanoparticles/thymine system [39].

AET and COOH of the thymine-COOH. The appearance of an additional O 1s peak at a binding energy of 532.7 eV for Au nanoparticles/thymine was assigned to the C–O bonding indicating the attachment of thymine-COOH on the Aunanoparticles/AET surface [39]. This XPS study helped to characterize the process of mercury interaction to thymine functionalized Au nanoparticles systems.

As with the studies of adenine with single crystal metal substrates, like Cu (111), the XPS study of adenine and thymine with PMA,  $[AuCl_4]^-$  and  $[Ag]^+$  provides some insight into the likely sites for metal coordination to a nucleic acid. This may provide a starting point to understand how metals interact with DNA, though as noted above, DNA is very different than a single nucleic acid.

## 5 Interaction of Hg (II) nanoparticles with plasmid DNA

DNA has unique self-assembling properties which makes it suitable forming spatially ordered 2-D, and 3-D structures [40]. This self-assembling property enables the design and fabrication of DNA nanostructures that provide programmable and predictable interactions with other biomolecules and various inorganic nanoparticles (NPs) [41]. The conjugation of metallic nanoparticles with DNA scaffold leads to the development of promising biosensors and bioelectronic devices.

X-ray photoelectron spectroscopic studies have shown that the electronic structure of DNA gets modified due to its interactions with the monovalent and divalent metal cations like silver (I) and mercury (II) [42, 43]. Plasmids are DNA molecules with a circular double-stranded structure having self-replication property without depending on chromosomal DNA for replication [44]. The circular plasmid DNA was isolated from the DH5 $\alpha$  bacterial cell and made to interact with the mercuric acetate salt solution. Both the mercury salt reacted plasmids and the pure plasmid were studied using scanning probe microscopy (SPM) and X-ray photoelectron spectroscopy [43]. The SPM images of the plasmid before and after its interaction with the mercury salt are shown in Figure 6.

The pure circular plasmid DNA [Figure 6 (b)] starts getting linearized after the reaction with the mercury salt as shown in Figure 6 (c and d), destructing the circular shape of the DNA [43]. The arrows in Figure 6 (c) points to the linear and circular DNA plasmid structure. In addition, formation of Hg nanoparticles within the DNA bases has also been noticed [43]. XPS results also indicate a strong interaction between the DNA bases and Hg nanoparticles.

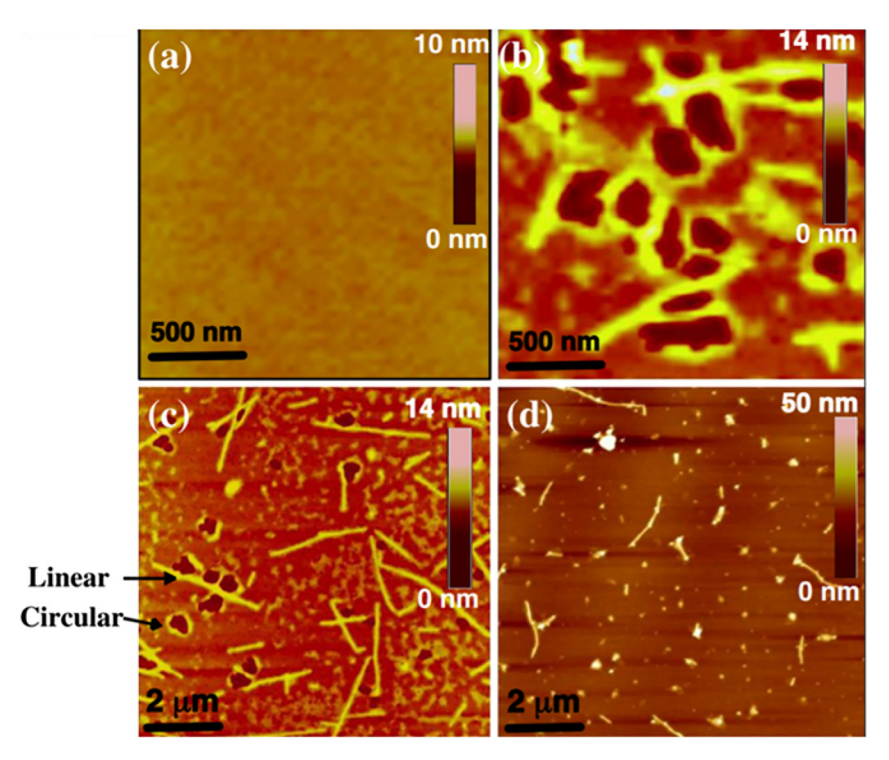


**Figure 6:** AFM images of (a) pure unreacted mica surface (b) pure plasmid DNA on the mica surface, after the interaction of plasmid with (c) 0.1 mM solution of mercuric acetate salt, (d) 10 mM solution of mercuric acetate salt [43].

Figure 7 (a–c) display XPS spectra of the elemental components of DNA such as carbon, oxygen, and phosphorus, respectively. These core levels were investigated both before and after the reaction of DNA with the mercuric salt. The XPS spectrum of C 1s core level of pure plasmid displayed components associated with –CH<sub>3</sub> group (282.4 eV), hydrocarbon component (284.6 eV), carbon bound to nitrogen (285.7 eV), carbon bound to an amino group (286.4 eV), and carbon bound to amide group (287.8 eV) [43]. Unlike the pure plasmid, mercury reacted plasmid showed enhancement of the features corresponding to the amino group and the amide group, suggesting strong perturbations to these components [43]. When mercury reacts with plasmid DNA, the nitrogen site of the nucleobases of the plasmid DNA

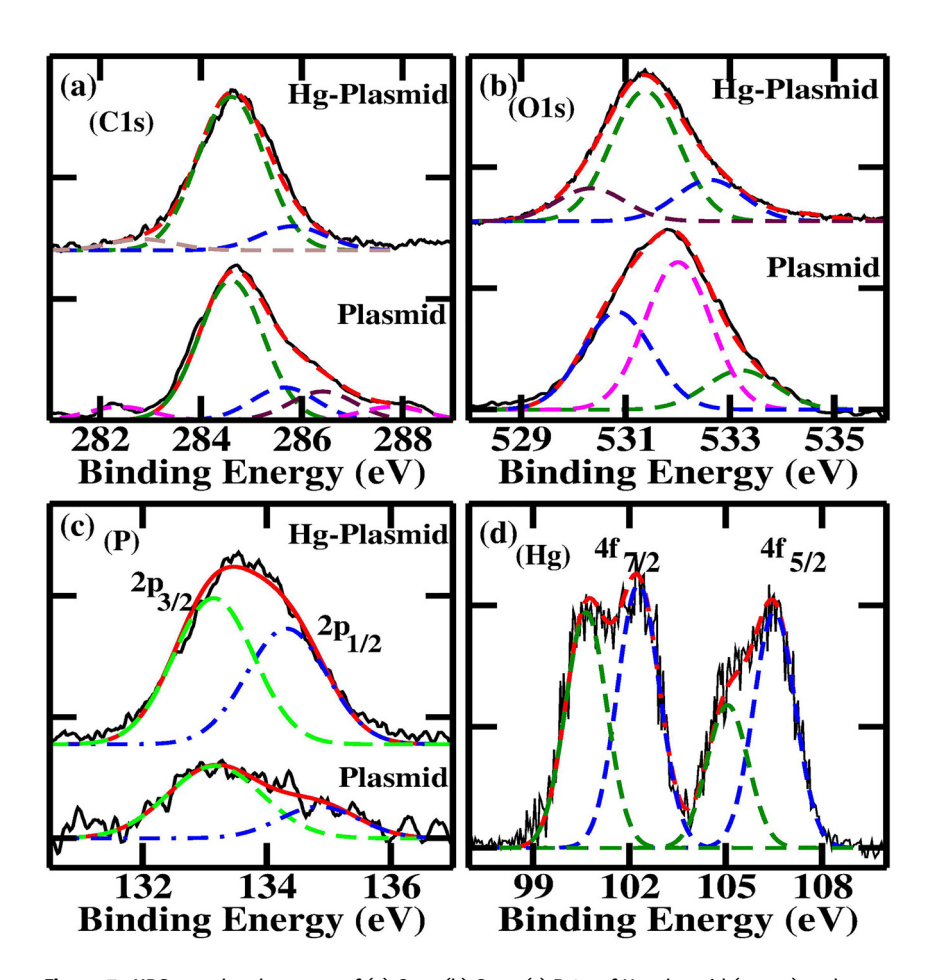


**Figure 7:** XPS core-level spectra of (a) C 1s, (b) O 1s, (c) P 2p of Hg-plasmid (upper) and pure plasmid (lower) and (d) Hg (4f) of Hg plasmid [43].

forms bonds with the mercury ions instead of carbon leading to the absence of amino and amide feature in C 1s and the appearance of an extra feature in N 1s as shown in Figure 8. Therefore, the perturbation in DNA means the selective interaction of the nitrogen of the nucleobases in the plasmid DNA with the Hg<sup>2+</sup> ions.

The O 1s core-level spectra of mercury reacted plasmid DNA displays a 0.6 eV shift towards the lower binding energies in comparison to the pure plasmid DNA suggesting that the electronegativity in oxygen is increased due to the mercury conjugation. This also brings into light the possible rupture of G-C pairing leading to the cleavage of H-bond after the Hg (II) conjugation with plasmid DNA. The mercury reacted plasmid DNA shows a similar feature as the pure plasmid DNA for the P core level spectra suggesting that there is no significant interaction of the mercury ions with the phosphodiester bond of the DNA. The Hg 4f core level spectrum of mercury reacted plasmid DNA as shown in Figure 7 (d) displays two features due to  $4f_{7/2}$  and  $4f_{5/2}$  at 101 and 106 eV respectively [43]. The binding energy features at 100.7 and 105.1 eV represent  $4f_{7/2}$  and  $4f_{5/2}$  atomic subshells of the metal purine pyrimidine complex. The features with Hg 4f binding energies at 102.3 and 106.5 eV were attributed to the hydrogen bond's cleavage between the purine and pyrimidine in the metal purine complex [43].

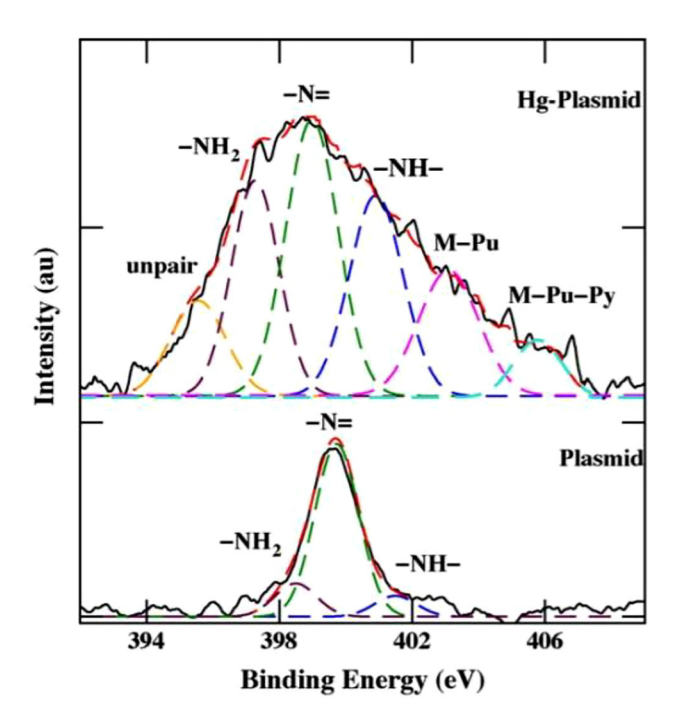


Figure 8: XPS core-level spectra of N 1s of Hg-plasmid (upper) and pure plasmid (lower) [43].

As shown in Figure 8, the N 1s spectrum of mercury reacted plasmid DNA is broad and has been fitted with six components. The imine component (-N=) shows a shift of 0.7 eV towards the lower binding energy in comparison to the unreacted plasmid DNA suggesting the perturbation due to the interaction of the nucleobases of the plasmid DNA with the mercury ions [43]. Ab initio calculations confirm that the transition metal cations with empty orbitals can accept electrons from the N7 atom of purines to form coordination complexes such as metal-purine-pyrimidine complexes [45]. In this study, when the imine structure gets protonated, guanine or adenine with the N7 atoms forms the metal purine pyrimidine complex corresponding to the N 1s core level feature at 405.6 eV. The N 1s core level feature at a binding energy of 403.1 eV for the metal purine complex is formed when the hydrogen bond in metal-purine-pyrimidine is broken. This XPS study [43] shows the severe perturbation of DNA molecules after its reaction with the mercuric salt. The linearization of the plasmid DNA and the shift in the binding energy of O 1s spectrum after Hg conjugation with plasmid DNA, leading to the cleavage of hydrogen bond via G-C rupture is also the cause of perturbation in the groups attached to the nucleobases [43].

### 6 Interaction of plasmid DNA with TiO<sub>2</sub> surfaces

The compatibility of  $TiO_2$  with different biomolecules along with its corrosion resistance properties and non-toxic nature could make this oxide an appropriate material for biomedical purposes [46]. The  $TiO_2$  was sputtered in the UHV with  $Ar^+$  ions with a flux of  $1\times 10^{13}$  ions/cm²s at an incident angle of 15°. Also,  $TiO_2$  was irradiated with the fluences of  $6\times 10^{15}$  and  $1.8\times 10^{16}$  ions/cm² for the duration of 10 and 30 min respectively [47]. The interaction of a plasmid DNA, which consisted of nearly 4361 base pairs isolated from the DH5 $\alpha$  bacterial cell, was made to interact with the  $TiO_2$  surfaces after the oxide was modified through various levels of ion bombardment [47].

As a complement to the X-ray photoemission studies, AFM was used to study the surface morphology before and after the interaction of the  ${\rm TiO_2}$  surface with DNA molecules, as shown in Figure 9 [47]. Figure 10 represents the power spectral density (PSD) function plots, derived from the AFM images of Figure 9, thus providing topographical parameters [48] for the virgin  ${\rm TiO_2}$  surface and  ${\rm Ar^+}$  ions irradiated  ${\rm TiO_2}$  surface.

The log-log representation of the power spectral density plots, as a function of wave vector ( $\kappa$ ), displays a plateau at low frequency followed by two frequency decay regions each separated by a unit order of  $\kappa$  magnitude. The points at which these regions intersect are related to the intermolecular separations ( $\xi$ ) and

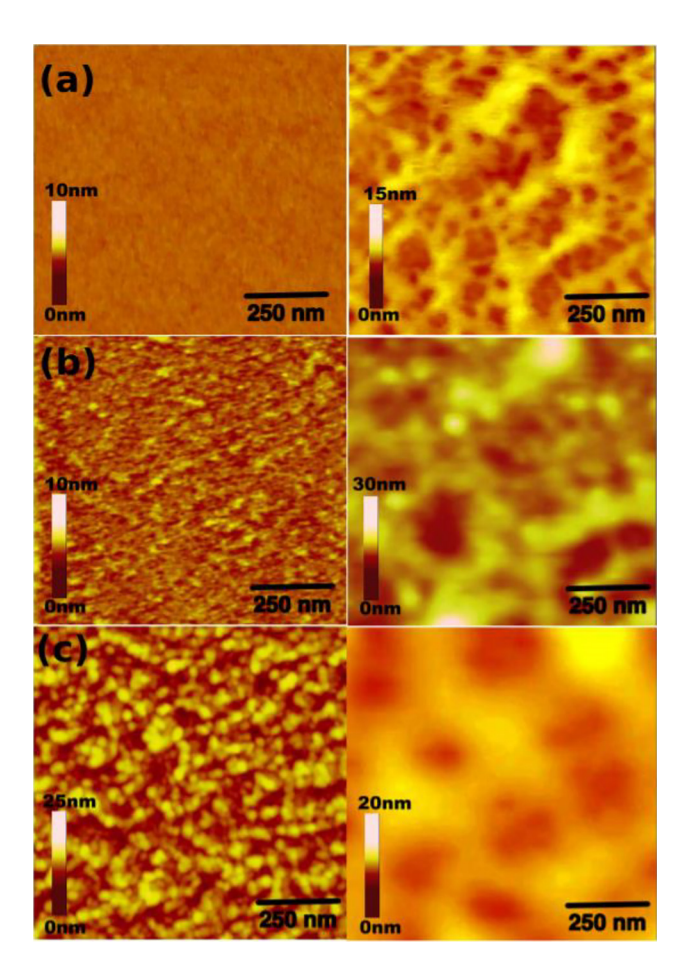


**Figure 9:** Left panel represents the AFM image of (a) virgin  $TiO_2$  surface, (b)  $TiO_2$  surface after being irradiated with Ar ions with the fluences of  $6 \times 10^{15}$  ions/cm<sup>2</sup>, (c)  $1.8 \times 10^{16}$  ions/cm<sup>2</sup>. The right panel represents the AFM images of (a) virgin  $TiO_2$  interacted with plasmid DNA, (b) plasmid DNA interacted with  $TiO_2$  after irradiated with the fluence of  $6 \times 10^{15}$  ions/cm<sup>2</sup>, and (c)  $1.8 \times 10^{16}$  ions/cm<sup>2</sup> [47].

persistence length (P) of the DNA. The increase in (P) denotes the increased stiffness of the DNA molecule [49]. The increase in  $(\xi)$  indicates the increase in biocompatibility and hydrophilicity because the measurement of  $(\xi)$  provides an indication of the area occupied by each DNA molecule [49]. Both  $(\xi)$  and (P) increase with an increased interaction with the  $TiO_2$  substrate. The inset shows the distribution of the average plasmid diameter, which increased with the increase in irradiation fluences of the  $TiO_2$  surface.

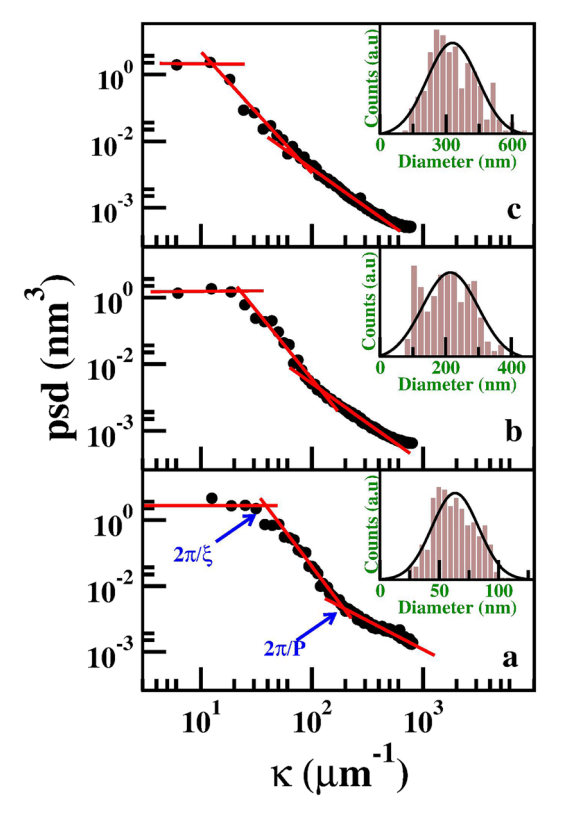


**Figure 10:** PSD plots for (a) virgin  $TiO_2$  surface interacted with plasmid DNA,  $TiO_2$  surface interacted with plasmid DNA after being irradiated with  $Ar^+$  ions with the fluence of (b)  $6 \times 10^{15}$  ions/cm<sup>2</sup> (c)  $1.8 \times 10^{16}$  ions/cm<sup>2</sup>. Inset represents the distribution of diameter of the plasmid DNA [47].

Figure 11 represents the Ti 2p region of the XPS spectrum from virgin TiO $_2$  and ion irradiated TiO $_2$  surfaces. As shown in Figure 11 (a), the XPS spectrum of the virgin sample shows two Ti 2p features at  $2p_{3/2}$  and  $2p_{1/2}$  which corresponds to the Ti $^{4+}$  coordination site/oxidation state. When the TiO $_2$  surface is irradiated with the flux of  $6 \times 10^{15}$  ions/cm $^2$ , along with Ti $^{4+}$  sites, Ti $^{2+}$  and Ti $^{3+}$  features are seen for both  $2p_{3/2}$  and  $2p_{1/2}$  states (Figure 11 (b)). Ti $^{4+}$  feature is the most significant in this case with a Ti $^{3+}$ /Ti $^{4+}$  ratio of about 0.3. However, when the TiO $_2$  surface is irradiated with  $1.8 \times 10^{16}$  ions/cm $^2$ , the Ti $^{3+}$  component becomes the most prominent (Figure 11 (c)) with the Ti $^{3+}$ /Ti $^{4+}$  ratio of about 4.1 (also shown in the inset). The Ar $^+$  ions irradiation on the TiO $_2$  surface causes the transfer of the two associated electrons from oxygen to the neighboring Ti atoms having unfilled 3d orbitals forming Ti $^{3+}$  and Ti $^{2+}$  state on the TiO $_2$  surface. Both the Ti $^{2+}$  and Ti $^{3+}$  component intensities increase with the increased surface damage [47]. This increase in oxygen vacancy states promotes the nucleation of Ti rich centers that induce the nanopatterning of the TiO $_2$  surface, consistent with the AFM studies as discussed in Figure 9.

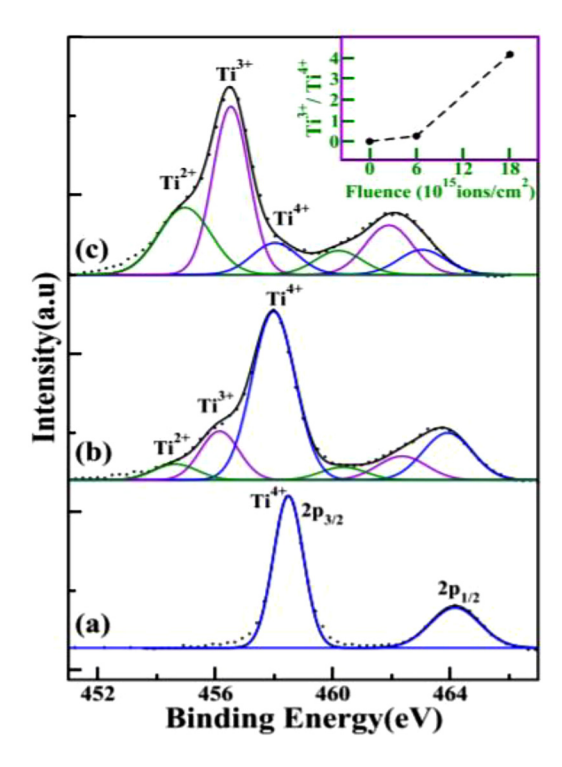
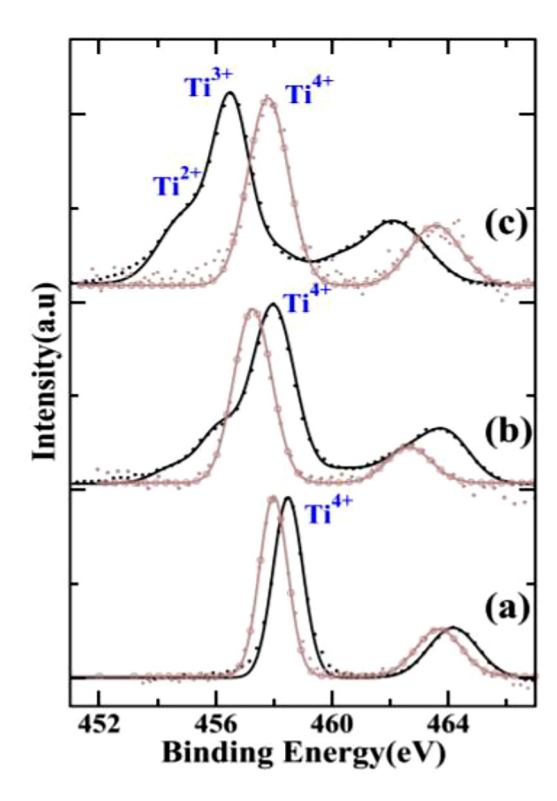


Figure 11: XPS spectra of Ti 2p region for (a) virgin TiO<sub>2</sub> surface, TiO<sub>2</sub> surface after being irradiated with Ar<sup>+</sup> ions with the fluences of (b)  $6 \times 10^{15}$  ions/cm<sup>2</sup> (c)  $1.8 \times 10^{16}$  ions/cm<sup>2</sup>. XPS intensities of the ratio Ti<sup>+3</sup>/Ti<sup>+4</sup> is shown in the inset [47].

Figure 12 depicts the spectra of the Ti 2p core level region for both the virgin TiO<sub>2</sub> surface and the ions sputtered surfaces that interacted with the plasmid DNA. As shown in Figure 12 (a), a shift in the Ti<sup>4+</sup> feature towards the lower binding energy is observed due to the interaction of the plasmid DNA with the virgin TiO<sub>2</sub> surfaces. This shift was attributed to the transfer of electrons to the surface from the negatively charged phosphate component backbone of the DNA. The Ti<sup>4+</sup> component is further shifted towards the lower binding energy when the surface irradiated with a fluence of  $6 \times 10^{15}$  ions/cm<sup>2</sup> interacts with the DNA as shown in Figure 12 (b). This shift indicates that more electrons are being transferred from DNA to the surface. The absence of both Ti<sup>3+</sup> and Ti<sup>2+</sup> states is observed as shown in Figure 12 (c) suggesting the surface has gained enough electrons from the phosphate component of the DNA causing saturation of both Ti<sup>3+</sup> and Ti<sup>2+</sup> after irradiation of the surface with a fluence of  $1.8 \times 10^{16}$  ions/cm<sup>2</sup> [47].

This study revealed that the interaction of TiO<sub>2</sub> surface with DNA brings conformational changes in the DNA structure and also indicated that the biocompatibility and hydrophilicity of TiO<sub>2</sub> surface changes with the increase in the ion bombardment fluence [47]. On the virgin TiO<sub>2</sub> surface, there is a relatively weak interaction between the surface and DNA because the transfer of electrons



**Figure 12:** The curve with circles represents XPS Ti 2p spectra after DNA interaction with (a) virgin TiO<sub>2</sub> surface, TiO<sub>2</sub> surface after being irradiated with the fluences of (b)  $6 \times 10^{15}$  ions/cm<sup>2</sup> (c)  $1.8 \times 10^{16}$  ions/cm<sup>2</sup>. For reference, XPS spectra (black dotted) without DNA interaction are also shown [47].

from the phosphate component of the DNA is small. This results in a small size with a small value of  $\xi$  and P. However, irradiation with a fluence of  $6 \times 10^{15}$  ions/cm² results in the increased charge transfer resulting in the saturation of  $\mathrm{Ti}^{2+}$  sites. The ions irradiated surface has oxygen vacancies which enhance the interaction between the DNA and ions leading to the larger size of plasmid DNA with the larger value of  $\xi$  and P. Furthermore, the irradiation of the surface with the fluence of  $1.8 \times 10^{16}$  ions/cm² results in the increase of the diameter of plasmid DNA along with the even larger values of  $\xi$  and P. Both the  $\mathrm{Ti}^{3+}$  and  $\mathrm{Ti}^{2+}$  states get saturated at this stage due to the charge transfer from the negatively charged phosphate backbone of the DNA. After irradiation, the increase in oxygen vacancies in the surface leads to the strong conjugation between the surface and the DNA [47].

#### 7 Silver with DNA

The study of the interaction of silver (I) with DNA is important because silver is a bioactive compound which acts as a mediator in the base pairing of noncanonical

DNA structure like guanine-guanine and cytosine-cytosine [50, 51]. XPS studies were carried out to study the interaction of i) silver cations with DNA, ii) *in situ* deposition of silver ions onto the DNA iii) DNA with fluorescent silver clusters [42].

Figure 14 is the diagrammatic representation of a fragment of DNA strand with cytosine (C), guanine (G), and thymine (T). The N 1s core level components  $N_{\rm I}$  (green) and  $N_{\rm II}$  (light green), in the XPS spectra of Figure 13 correspond to the similarly colored N indicated in the diagrammatic representation of a DNA fragment in Figure 14. In a similar fashion, the N 1s core level components  $O_{\rm I}$  and  $O_{\rm II}$  in the XPS spectra of Figures 13 and 15 corresponds to blue and light blue colored O indicated in the diagrammatic representation of a DNA fragment in Figure 14. As shown in Figure 13, in the case of pure DNA with r = 0.0, the peak observed at the binding energy of 399.4 eV ( $N_{\rm I}$  component) was assigned to the nitrogen atoms in the C=N-C and C-NH<sub>2</sub>. The peak observed at the binding energy of 400.8 eV ( $N_{\rm II}$  component) was assigned to the nitrogen in N-C=O and N-C-O. Likewise, in the

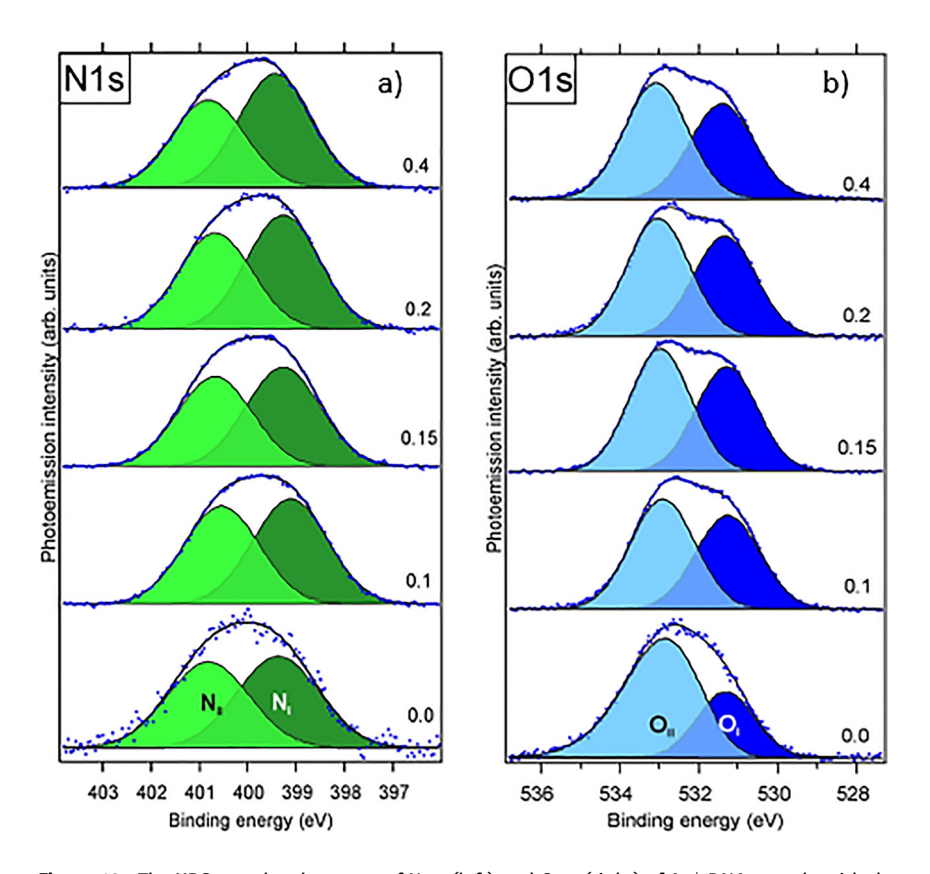


**Figure 13:** The XPS core-level spectra of N 1s (left) and O 1s (right) of Ag $^+$ -DNA sample with the numerical value of r on the right of each spectrum, where  $r = [Ag^+]/[DNA_{base}]$  [42].

Figure 14: A diagrammatic representation of a fragment of DNA strand with bases cytosine (C), guanine (G), and thymine (T) [42].

case of the O 1s spectrum, the peak of the  $O_I$  component was observed at binding energy 531.3 eV which is assigned to the groups P=O, C=O, and P-O $^-$  of DNA. The  $O_{II}$  peak observed in the O 1s core level spectrum of the pure DNA is assigned to the water present on the HOPG (highly oriented pyrolytic graphite) substrate used in the preparation of the thin films of silver-DNA complexes [42].

What becomes evident from Figure 13, is that with the increase in the value of  $r = [Ag^+]/[DNA]$ , a redistribution of  $N_I$  and  $N_{II}$  components occurs in the N 1s spectra. It was observed that the  $N_{II}$  component shifts towards the lower binding energy. This shift was attributed to the binding of  $N_{II}$  sites with the silver cations. In the case of oxygen, for  $r \ge 0.1$ , the XPS spectrum of O 1s showed no significant change suggesting no interaction between the oxygen atoms and  $Ag^+$  ions [42].

The *in-situ* deposition of the atomic silver onto a DNA film, in the spectrometer vacuum chamber, resulted in significant changes to the XPS spectra. As shown in Figure 15, the XPS spectra of O 1s, in this case, show redistribution of  $O_I$  and  $O_{II}$  intensities. The shift of the  $O_{II}$  component towards the lower binding energy was attributed to the interaction of oxygen of the phosphodiester bond/deoxyribose of DNA with silver atoms. The XPS spectra of N 1s shows a similar spectrum as DNA-Ag $^+$ . However, for the third case, in the XPS study of the HPLC (High-Performance Liquid Chromatography) purified complex of the fluorescent silver cluster with DNA, the spectral changes in O 1s and N 1s spectra were not observed [42].

Thus, the XPS spectra of three different types of silver-DNA complexes were studied and this helps in understanding the DNA metallization mechanism for silver which will aid in the development of metal-bio interfaces. It has been noted that silver (Ag) DNA compounds are potential materials for DNA-templated silver nanorings [52].

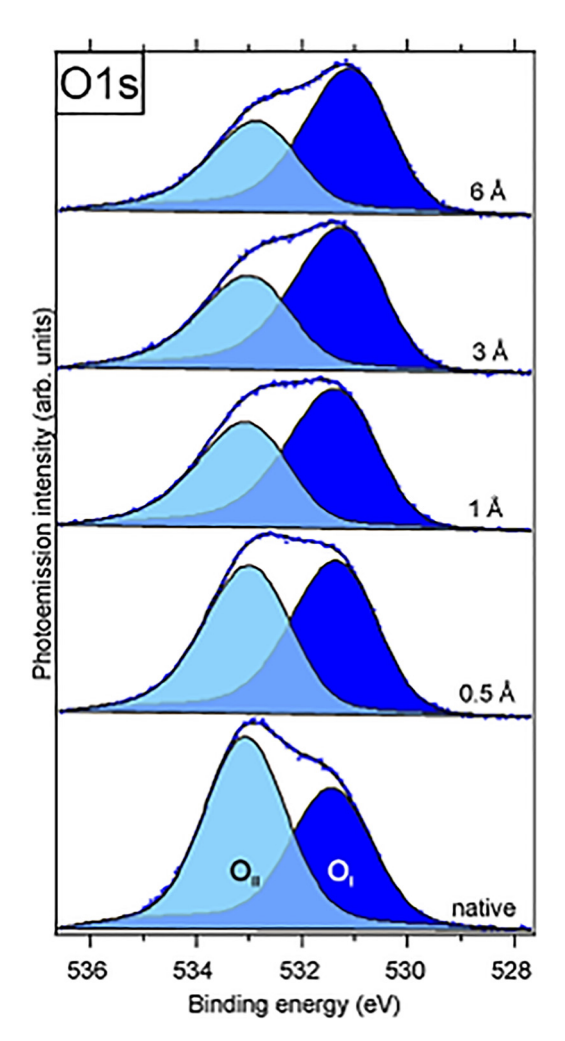


Figure 15: The XPS core-level spectra of O 1s due to gradual deposition of atomic silver onto DNA in UHV. The numerical value on the right is nominal layer thickness [42].

### 8 DNA interactions with Al (III) and Fe (III) cations

As mentioned above, DNAs are basically large polymeric molecules consisting of various nucleotides (i.e., adenine (A), thymine (T), guanine (G), or cytosine (C)) and have a negatively charged phosphate group. Hence it is possible to condense these molecules by neutralizing the negative charges present in the phosphate group by means of various metallic or organic cations [53–55]. The compaction of the DNA molecules having intramolecular condensation is crucial for the development of non-viral gene delivery vectors [56].

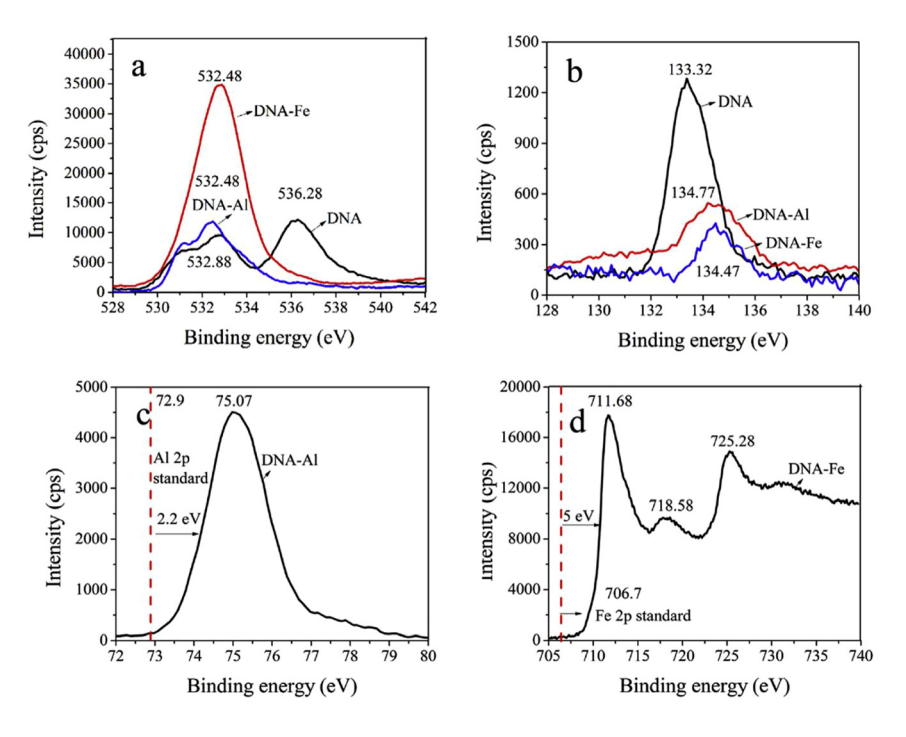


Figure 16: XPS core-level spectra of O (a), P (b), Al (c), and Fe (d) both before and after the interactions with salmon testes DNA [56].

This condensation or the compaction of DNA can also occur in the presence of trivalent metal cations such as  $Fe^{3+}$  and  $Al^{3+}$  in an aqueous medium. The phenomenon of aggregation or the compaction of the DNA molecules influenced by the environmentally relevant metal cations such as  $Al^{3+}$  and  $Fe^{3+}$  was investigated by C. Qin et al. [56]. DNA from salmon testes was employed for their study, and the compaction phenomenon was investigated with the X-ray photoelectron spectroscopy. The XPS spectra and feature assignments is depicted in Figure 16.

The compaction of DNA, by forming DNA-Fe (III) and DNA-Al (III) complexes, were investigated by analyzing core-level X-ray photoemission spectra of O, P, Fe, and Al [56]. The observed O 1s peak at 531.3  $\pm$  0.2 eV was assigned due to the oxygen present in the nucleobases and pentose sugars. And the peak at around 532.7  $\pm$  0.2 eV was assigned due to the oxygen from the phosphate backbone. The O 1s peak observed at 532.88 eV was assigned due to the oxygen from -0-P group of the phosphate backbone of the DNA before the interactions with Fe (III) and Al (III) metal cations. O 1s peak at 536.28 eV could be attributed to the water molecules present in the DNA samples. After the interaction of DNA with Al (III) and Fe (III), the O 1s peak at 536.28 eV vanished due to the adequate drying of the DNA samples.

The peak at 532.88 eV of the O 1s spectra shifted to 532.48 eV ( $\Delta$  = 0.4 eV) after the DNA interacted with Fe (III) and Al (III) cations. This shifting of the O 1s core level binding energies may be assigned to the formation of the DNA-Fe<sup>3+</sup>/Al<sup>3+</sup> complexes that occurred at the backbone of the DNA. The supply of an electron density from the Fe and Al metal ions to the DNA backbone sites results in a decrease the O 1s binding energy. On the other hand, for P  $2p_{3/2}$  spectra, the binding energies increased from 133.32 to 134.77 eV ( $\Delta$  = 1.45 eV) and 134.47 eV ( $\Delta$  = 1.15 eV) for DNA-Al (III), and DNA-Fe (III) complexes respectively which could be attributed to the formation of the strong electrostatic binding between negatively charged phosphate backbone and the metallic cations. The shifting of the core level binding energies for Al 2p and Fe 2p were 2.2 and 5.0 eV respectively which were due to the complex formations of Al<sup>3+</sup> and Fe<sup>3+</sup> with the negatively charged oxygen present in the phosphate group in the DNA.

These studies based on XPS, suggest an influence, by the trivalent metallic cations such as Al<sup>3+</sup> and Fe<sup>3+</sup>, on the compaction of DNA molecules [56]. More generally, this evidence of a strong interaction of trivalent metallic cations with DNA could aid in the development of sensors for these metal ions as well as metal-bio interfaces. The metal cation interaction with DNA is not restricted to only trivalent metallic cations, as discussed next, so sensor specificity might be problematic.

# 9 Metal cation-induced deformation of DNA self-assembled monolayers on silicon

For the compaction or condensation of DNA molecules, monovalent and divalent metal cations play an important role by reducing the Coulombic repulsion between the phosphate backbones within and between DNA molecules. These metal cations may induce compaction of the DNA molecules as well as induce various deformations such as bending, twisting, and change in groove width [57]. An investigation was carried out using X-ray photoelectron spectroscopy by Hidehiko et al. [57] on the DNA adsorption on the silicon (Si) surface as well as investigate interactions with alkali and alakali earth metal cations such as Na<sup>+</sup>, K<sup>+</sup>, Mg<sup>2+</sup>, and Ca<sup>2+</sup>. In their study, the immobilization of the DNA strands on the bare clean Si wafer was performed using 1-decene and undecylenic acid (9:1 M ratio), and afterward, the surface was activated using 1-ethyl-3[3-(dimethylamino)-propyl] carbodiimide (EDC) and N-hydroxysuccimide (NHS).

In this study [57], the amino-functionalized ssDNA (5'-NH<sub>2</sub>-C<sub>6</sub>-TCG ATC TGA CGT CAG TCA AA-3') with a saline solution containing salts such as NaCl, KCl, CaCl<sub>2</sub>, and MgCl<sub>2</sub> was allowed to react with a silicon/silicate surface. The

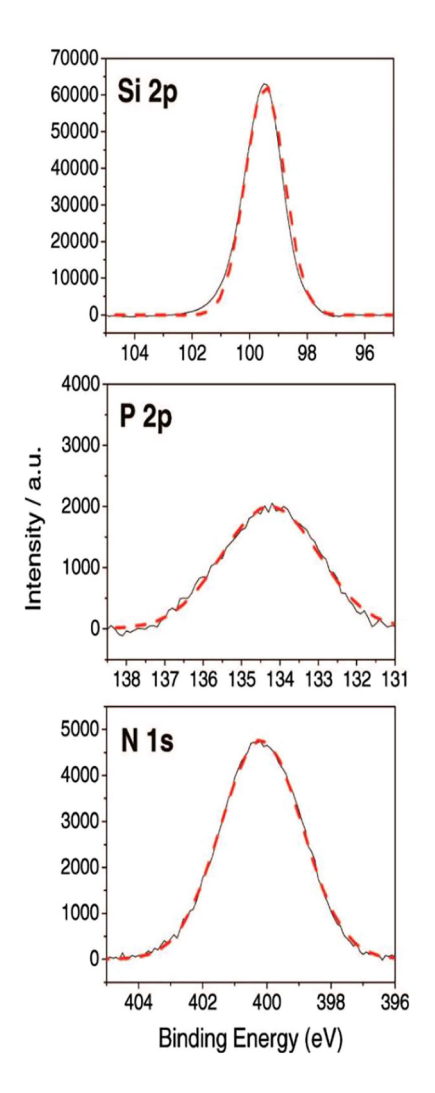


Figure 17: The core-level XPS spectra of a DNA self assembled monolayer (SAM) on silicon substrate [57].

immobilization of the DNA strands on the silicon surface was characterized by X-ray photoemission spectroscopy, as shown in Figure 17. The peaks of phosphate (P) and nitrogen (N) constitute enough evidence for the presence of DNA strands on the silicon/silicate surface. Interaction of the DNA molecules with different cations exhibited almost the same XPS P 2p and N 1s core level profiles. The observed P 2p XPS peak at a binding energy of 134.3 eV indicates the presence of the phosphate backbone of the DNA on the Si surface as the binding energy of P 2p peak is in close

agreement with the reported value [58, 59]. The slight deviation of the Si 2p peak at 99.5 eV represents oxide formation on the surface, as shown in Figure 17. The N 1s peak observed at 400.2 eV was assigned to nonconjugated nitrogen present in the amine-functionalized DNA molecules which is closer to the reported value [60]. The absence of N 1s peak at 402.6 eV (N-O) indicated the efficient amide coupling of amine-functionalized DNA to the carboxyl groups present on the silicon surface [61]. The sum-frequency generation (SFG) spectroscopy studies on the DNA functionalized silicon surface in the influence of different metal cations revealed that the distortion of the linker monolayer decreased in the order of  $Mg^{2+} > Ca^{2+} > Na^+ \approx K^+$  and this is similar to the fact that the divalent or trivalent cations interact more strongly with the negatively charged phosphate backbone of the DNA molecules in comparison to monovalent cations. The interaction of the metal cations with the DNA molecules was further characterized with XPS as shown in Figure 18. After interacting strongly with the DNA, the characteristic peaks for Ca 2p observed at 342 eV, and by deconvoluting the Mg 2p core-level spectra, peaks at binding energies of 52 and 55 eV were found. These two deconvoluted Mg 2p core-level features were assigned on the basis of the coupling of the cations with the negatively charged phosphate groups (higher energy), and with the nucleosides (lower energy) respectively. It was observed that the interaction of the DNA with Mg<sup>2+</sup> is more persistent than with the  $Ca^{2+}$ , as the ratio between the signals from the cation to the phosphate (P) is much higher in the case of Mg 2p (Mg/P  $\sim 1.45$ , Ca/P  $\sim 0.04$ ). The deformation of the DNA molecules, influenced by the metal cations, plays a crucial role in the charge neutralization of the negatively charged phosphate backbone and the drastic conformational changes in the DNA structures. In the DNA molecules having all types of nitrogenous bases, the interaction of the metal cations occurs mostly at the Guanine bases and the distribution of the charges around the DNA molecules become inhomogeneous, which eventually causes the DNA molecules to bend significantly on the Si surface. These deformations are much more significant for the divalent cation  $Mg^{2+}$  than the monovalent cation  $Na^+/K^+$  [57]. This study gives insights into the fabrication of DNA micro-arrays with maximum probe density.

# 10 Reversible adsorption-desorption at the interface of DNA with ZrO<sub>2</sub> nanoparticles

The immobilization of the DNA molecules on the solid surface has attracted immense attention due to its applications in the field of DNA-based bio-chip, DNA computers and DNA modified electrode systems [62–64]. Zirconia  $(ZrO_2)$  based spectroscopic study of the adsorption and desorption of DNA was carried out by

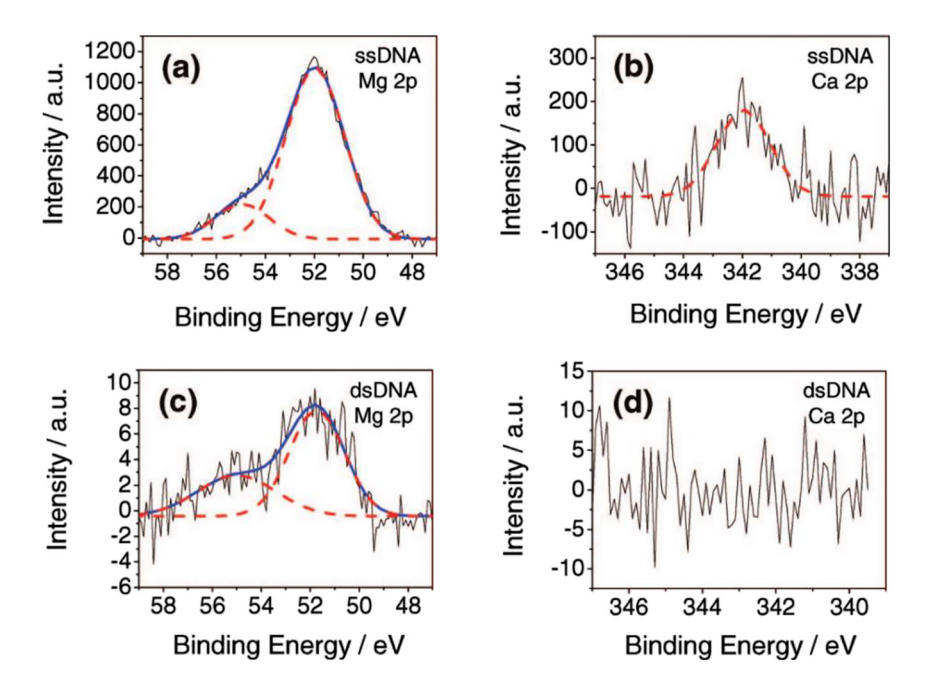


**Figure 18:** The core-level XPS spectra of silicon modified with DNA SAMs upon immobilization in the presence of (a)  $MgCl_2$  (b)  $CaCl_2$  and after hybridization with complementary strands in the presence of (c)  $MgCl_2$  or (d)  $CaCl_2$  [57].

S.-Q. Liu et al. [65] where the zirconia nanoparticles (NPs) were prepared by means of the sol-gel method. The adsorption of calf thymus DNA was performed by dipping the ZrO<sub>2</sub> coated glassy carbon (GC) electrode into the DNA solution.

The adsorption of DNA molecules onto the zirconia coated GC electrode was characterized by both differential pulse voltammetry (DPV) and X-ray photoelectron spectroscopy as shown in Figures 19 and 20 respectively. As shown in Figure 19, there is a significant increase at the peak current for GC-ZrO<sub>2</sub>-DNA electrode with  $Co(phen)_3^{3+}$  (Figure 19 (c)) and decrease in the peak current for GC-ZrO<sub>2</sub> electrode (Figure 19 (b)) in comparison to the GC electrode (Figure 19 (a)), suggesting the role of  $ZrO_2$  as a connecting component or the bridge for the process of DNA immobilization onto the GC electrode surface. XPS was performed on the  $ZrO_2$  both before and after the interaction with calf thymus DNA and the XPS peak for the P ZP from the phosphate backbone of the DNA molecule was observed at 132.95 eV only when the  $ZrO_2$  coated GC electrode was immersed in the DNA solution, and no signal was found without the binding as shown in Figure 20 which agrees to the idea of immobilization of DNA on  $ZrO_2$  NPs. For the desorption of the

DNA from the  $ZrO_2$  NPs, KOH solution was utilized by immersing the modified electrode for 10 h. And again, for the adsorption of the DNA molecules to the  $ZrO_2$  NPs, the previously mentioned method was applied, and a similar current response was observed [65].

It has been noted that the reversible DNA adsorption-desorption process with the zirconia NPs has potential for the preparation of reusable bio-chip and information storage devices [65], although we note that the write speed would be slow.

### 11 Cu<sub>2</sub>O@NCs-DNA

Chitin is a polysaccharide occurring naturally in the arthropod exoskeleton and fungi/yeast cell wall [66]. Nano-chitosan particles (NCs) exhibit good

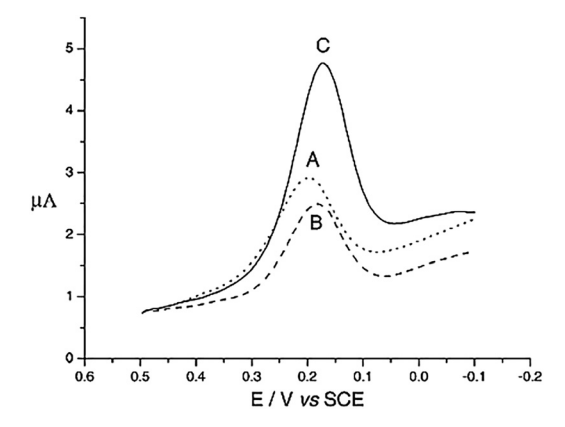


Figure 19: The differential pulse voltammetry of (a) GC electrode, (b) GC-ZrO<sub>2</sub> electrode and (c) GC-ZrO<sub>2</sub>-DNA electrode with Co(phen)<sub>3</sub><sup>3+</sup> [65].

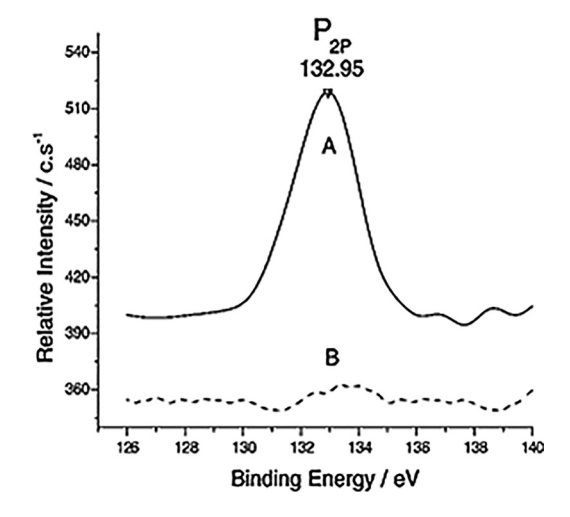


Figure 20: The core-level XPS spectra of P 2p of (a) the ZrO<sub>2</sub> nanoparticles (NPs) after functionalized with calf thymus DNA and (b) the ZrO<sub>2</sub> NPs without DNA [65].

biocompatibility and might be used as a biosensor to immobilize the biomolecules [67, 68].  $Cu_2O$  has been explored as a possible electrochemical sensor such as L-tyrosine sensors [69] and enzyme-free glucose sensors [70]. Based on the unique features of both the nano-chitosan particles and  $Cu_2O$ , Liu et al. [68] fabricated a highly sensitive electrochemical biosensor ( $Cu_2O@NCs$ ) using NCs as the shell and  $Cu_2O$  as the core structure.

Figure 21 represents the proposed electrochemical sensor scheme based on  $Cu_2O@NCs$  nanocomposites. The high affinity between the DNA strands and  $Cu_2O@NCs$  favors the adsorption of DNA strands to  $Cu_2O@NCs$ . The  $Cu_2O$  was placed within the nanocomposite. The combined  $Cu_2O$  chitosan nanosphere provides active sites for DNA molecule surface attachment. This biosensor detects  $Hg^{2+}$  ions through the formation of the T- $Hg^{2+}$ -T complex [68].

XPS analysis was used to study the composition of the nanomaterial before and after the biosensor interaction. As shown in Figure 22, the core level spectra of Cu 2p were observed in all the samples. The peak observed at 932.2 eV was assigned to Cu  $2p_{3/2}$  and the peak observed at 951.9 eV was assigned to Cu  $2p_{1/2}$ . After the combination of NCs with the Cu<sub>2</sub>O nanostructure, XPS signals for C 1s and N 1s were also studied. The core-level spectra of C 1s contain three peaks, i) at 284.6 eV attributed to C–C/C–H bond, ii) at 286.2 eV attributed to C–N bonds, and iii) at 288.2 eV attributed to the carboxyl groups [68].

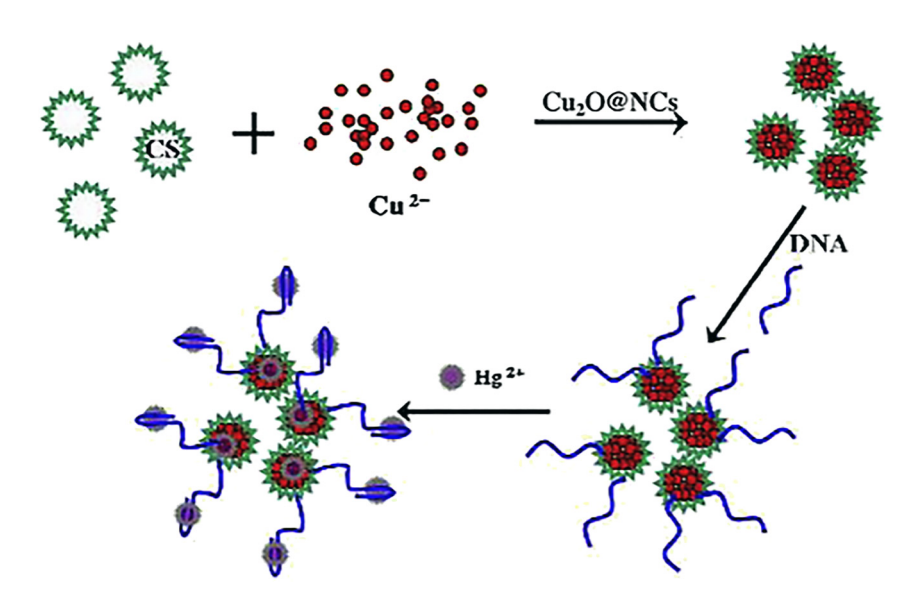


Figure 21: A schematic representation of an electrochemical biosensor for the detection of  $Hg^{2+}$  ions based on  $Cu_2O@NCs$  nanocomposites [68].

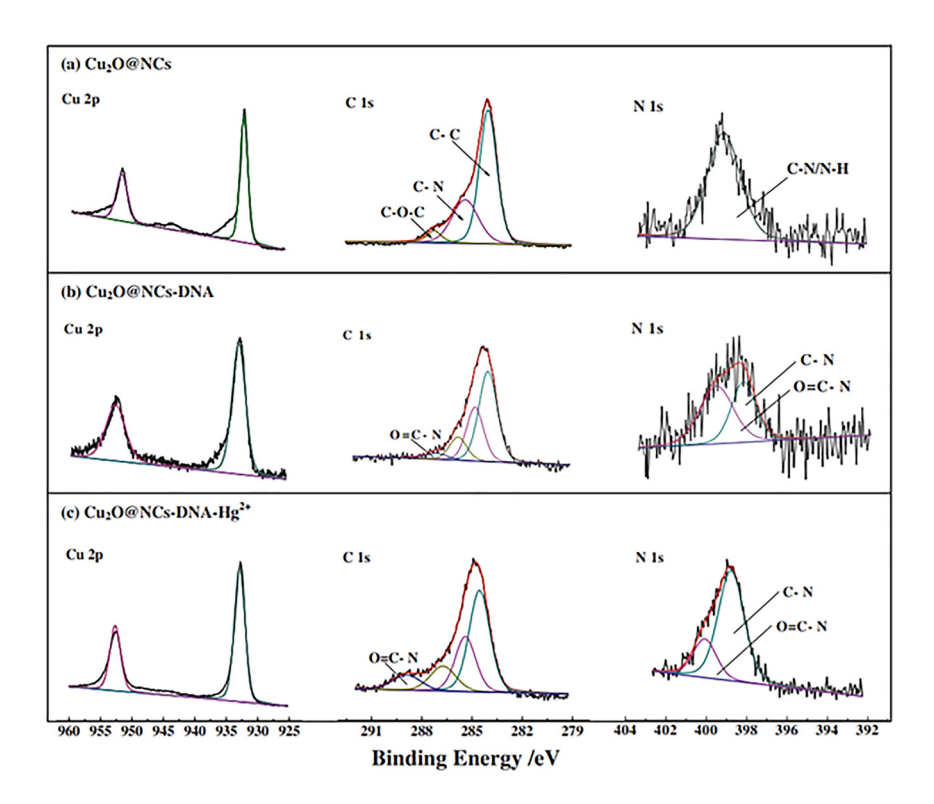


Figure 22: The XPS core-level spectra for Cu 2p, C 1s, and N 1s for (a) Cu $_2$ O@NCs, (b) Cu $_2$ O@NCs interacted with DNA, (c) Cu $_2$ O@NCs-DNA with Hg $^{2+}$  [68].

When the DNA strands were immobilized onto the surface of  $\text{Cu}_2\text{O}@\text{NCs}$ , a new C 1s peak was observed at 289.0 eV which was attributed to the N–C=O group of the DNA. These results favor the anchoring of the single-stranded thymine (T) rich DNA on the surface of the  $\text{Cu}_2\text{O}@\text{NCs}$  composite. After the detection of the  $\text{Hg}^{2+}$  ions, increase in the intensity of the N–C=O group was observed. This behavior was attributed to the double-stranded DNA chains that were produced after the coordination of the T-Hg<sup>2+</sup>-T between the  $\text{Hg}^{2+}$  ions and the DNA strands. The core-level XPS spectra of the Hg  $^4$  signal show peaks at 99.4 eV attributed to Hg  $^4$  and a peak of 103.3 eV attributed to Hg  $^4$  Based on the XPS results, the change in the electronic structure of the different components of the nanocomposites supports the claim that  $\text{Cu}_2\text{O}@\text{NCs}$  can be used as an electrochemical biosensor for the detection of Hg [68].

### 12 The Bi<sub>2</sub>O<sub>3</sub>-DNA template

The properties of  $Bi_2O_3$  such as high dielectric permittivity, a large energy band gap, a high refractive index, and excellent photoluminescence make bismuth oxide suitable for various microelectronics and optical devices [71, 72], but the biocompatibility is not well understood. Indeed, the study of bismuth compounds with bio molecules is a good starting point to the investigation of other heavy metals and heavy metal compounds. The unique property of nanowires and nanotubes to efficiently carry charges and excitons [73], could possibly make bismuth oxide nanowires a suitable building block for optoelectronic devices. As such, the interaction characteristics of bismuth oxide with biomolecules is of interest if optoelectronic bismuth oxide biosensors are going to be valuable. DNA does provide a scaffold for  $Bi/Bi_2O_3$  nanowires. The DNA templated growth of  $Bi/Bi_2O_3$  nanowires was obtained by using the electrochemical reduction of Bi (III) at the surface of an n-type Si electrode [74]. The self-assembling property of DNA templates along with its programmed base sequence can be used to construct complex structures [75].

The XPS spectra of Bi 4f electron is shown in Figure 23. When the bismuth ions present in an electrolytic solution reacts with DNA, Bi nanowires are likely to deposit on the Si substrate. The evaporation of the electrolytic solution in air reoxidized the Bi nanowires forming  $\mathrm{Bi_2O_3}$ . The oxide layer of a thickness in the region of 4 nm was reported when metallic Bi wires were exposed to the air for 4 h [76]. In this work [74], the complete oxidation of the wires is expected as the thickness of the wire is about 5 nm. Therefore, the peak position at binding energies 158.7 and 163.9 eV corresponds to Bi  $4f_{7/2}$  and Bi  $4f_{5/2}$  respectively for  $\mathrm{Bi_2O_3}$ , and the singlet peaks at the binding energy of 150.3 and 153.2 eV were assigned to Si 2s [74]. The result of this study showed that the dominant component of the material was  $\mathrm{Bi_2O_3}$  which can therefore be used in the construction of complex chemical architectures.

#### 13 Uranium and urania – eDNA

Biopolymers such as polysaccharides, polypeptides, and nucleic acids are constituents of bacterial extra polymeric substances (EPS) [77]. Indeed, extracellular DNA (eDNA) is one of the major extra polymeric substances (EPS) components [78]. Hufton et al. [79] studied the mechanism involving eDNA as a contributor in the process of uranium phosphate mineral formation, which is one of the key components for the process of biomineralization of uranium.

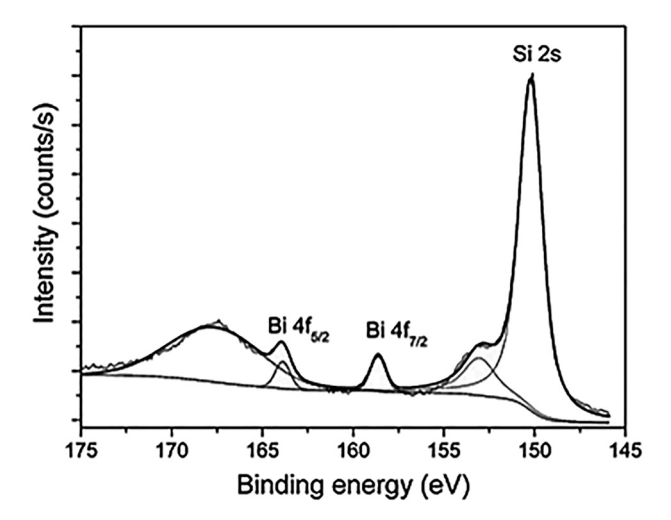


**Figure 23:** The XPS spectrum for Bi 4f and Si 2s core levels for Bi/Bi $_2$ O $_3$  nanowires on Si electrode [74].

eDNA was chosen for study because i) the presence of phosphate groups in eDNA helps in quantifying the precipitation of uranium and ii) ePO $_4$  can be enzymatically released from eDNA. ePO $_4$  when reacted with uranium results in the formation of uranium phosphate minerals [79]. The hypothesis of this study [79] was that ePO $_4$ , at acidic conditions would effectively bind the U(VI) species that are highly mobile. The results of the ePO $_4$  studies were also compared with aPO $_4$ , an abiotic precipitate obtained from NaH $_2$ PO $_4$  [79]. The XPS studies were, as shown in Figure 24, carried out on the uranium minerals that were formed using aPO $_4$  and ePO $_4$ .

The XPS spectrum showed the presence of uranium, phosphorus, oxygen, chlorine, and sodium. The use of carbon tape during the preparation of the sample made it difficult to identify the carbon peak, however, a high-resolution scan showed carbon peaks in  $ePO_4$  minerals. The XPS peaks of carbon at 285, 286.49, and 288.88 eV were attributed to the carbon tape [79]. The carbon peaks were absent in  $aPO_4$  minerals as the abiotic reaction between  $aPO_4$  and uranium had no presence of carbon. The carbon peak at 287.91 eV is attributed to the carbon-oxygen double bond in the  $ePO_4$  mineral. The satellite peaks at 293.24 and 295.95 eV corresponds to the residual impurities of carbon that remained after the synthesis of  $ePO_4$  [79].

The core-level XPS spectra of U 4f of uranium mineral synthesized using aPO<sub>4</sub> and ePO<sub>4</sub> shows the peak separation of 10.87 eV between  $4f_{7/2}$  and  $4f_{5/2}$ . The presence of the higher peaks than the main  $4f_{5/2}$  and  $4f_{7/2}$  peak is attributed to the

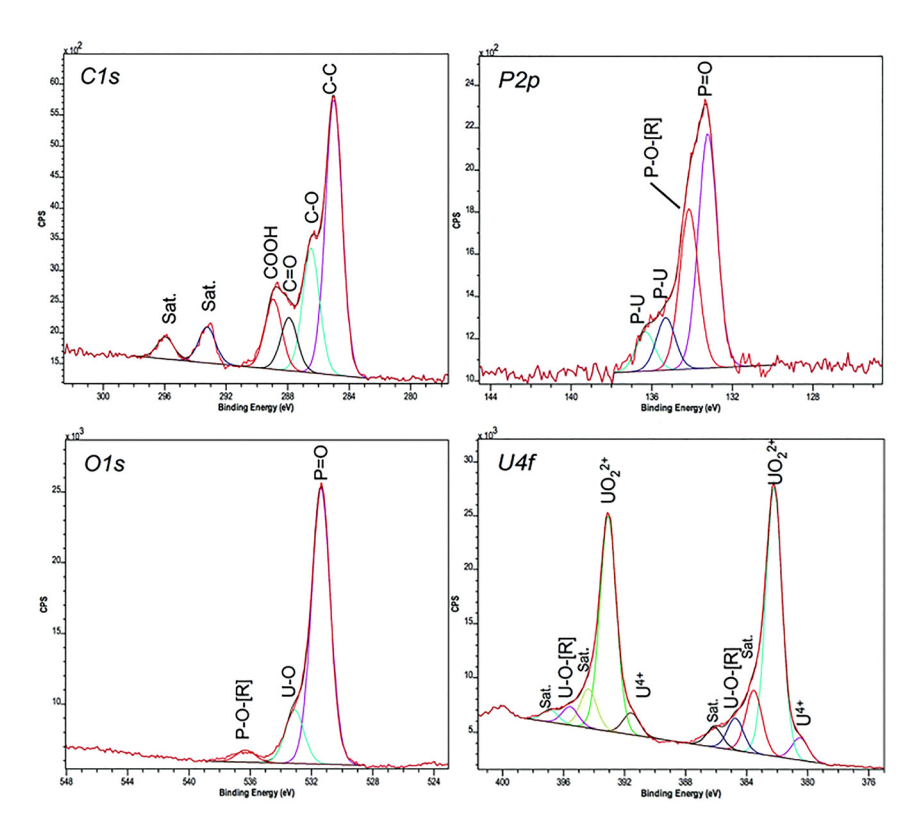


**Figure 24:** The XPS spectra taken at the C 1s, P 2p, O 1s, and U 4f core levels for uranium minerals formed using ePO4 [79].

interaction of the valence electrons with the photoelectrons during the process of photoexcitation [79].

The uranium 4f core level XPS region, for the  $UO_2(NO_3)_2.6H_2O$ , a U(VI) species, shows two additional features for both  $4f_{5/2}$  and  $4f_{7/2}$  core levels. The highest satellite peak indicates that most of the uranium in the minerals is present in the VI oxidation state. The other remaining high energy peaks could be the satellite peak or the peaks formed during the interaction of uranium with the phosphate group. The XPS analysis helped elucidated the fact that the uranium minerals produced using  $ePO_4$  are probably due to the presence of nitrogen and carbon impurities in  $ePO_4$  than  $aPO_4$ . Although, due to the presence of impurities, the minerals could not be identified clearly but the uranium mineral formed was identified as a uranium phosphate mineral [79]. This study helps to explain the role of  $ePO_4$  in the complexation and mineralization of uranium in the presence of eDNA and thus eDNA plays a vital role in the biomineralization of uranium.

# 14 Bio-metal interface interaction of S-layer protein with Cu and Fe

XPS was used to study the interaction between the surface layer proteins of a regular bacteria with metals like Cu and Fe [80]. Figure 25 shows the N 1s core-level spectra of the native surface layer proteins and surface layer proteins after the deposition of Cu and Fe with varying nominal thickness. At 400.1 eV, the N1 feature can be seen which corresponds to the nitrogen atoms in peptide bonds, amide bonds, or the amine groups in the side chains [80]. With the increase in nominal thickness, an additional N2 feature appears at 398.4 eV corresponding to the C=N bond. In the case of SL-Fe, a third feature N3 is observed at 397 eV corresponding to the C=N or Fe=N bonds [80].

Figure 26 shows the O 1s core-level spectra of the native surface layer proteins and surface layer proteins after the deposition of Cu and Fe with varying nominal thickness. In the case of surface layer proteins with Fe, a new feature O1 is detected at 530 eV which could be the peak corresponding to the iron oxides [81].

Figure 27 shows the photoemission line shape evolution of the Fe 2p core-level spectra with increasing metal coverage. The increase in the intensity of the Fe 2p feature A, with an increase in the thickness of the Fe deposition, at the binding energy of about 707 eV, indicates the possibility of elemental Fe being present [82]. The satellite features at the higher binding energy in Fe 2p spectra correspond to the +2 or/and +3 oxidation state of Fe. This indicates that the iron is oxidized during its interaction with the protein [80]. Therefore, this study compares the stability of the protein hybrid system which helps in understanding the protein metal interactions. The hybrid with copper appears to be more stable in comparison to the hybrid with iron as iron decomposes to form carbides, oxides, nitrides, and cyanides [80].

### 15 Brown marine microalgae

The treatment of the wastewater contaminated with toxic heavy metal ions can be done by the process of biosorption [83]. Biosorption is a technique in which the functional group or ligands of the biological materials can be used to form complexes with heavy metal ions [84]. Photoemission studies were carried out to study the mechanism of bio adsorption of heavy metal cations such as Cd, Ni, and Pb on the chemical groups present on the cell wall of *Sargassum vulgaris*, brown marine macroalgae [85].

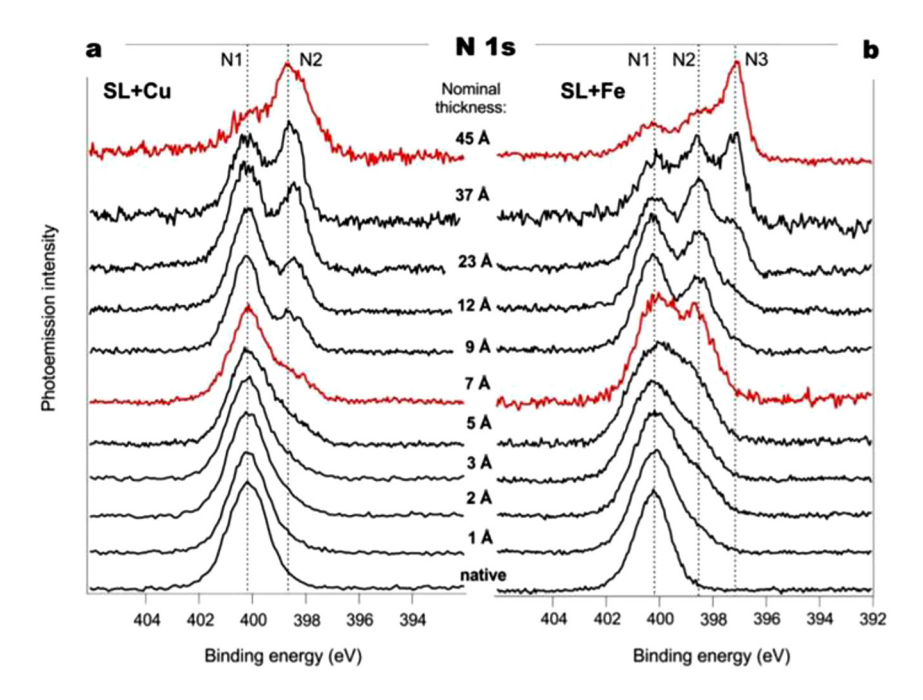
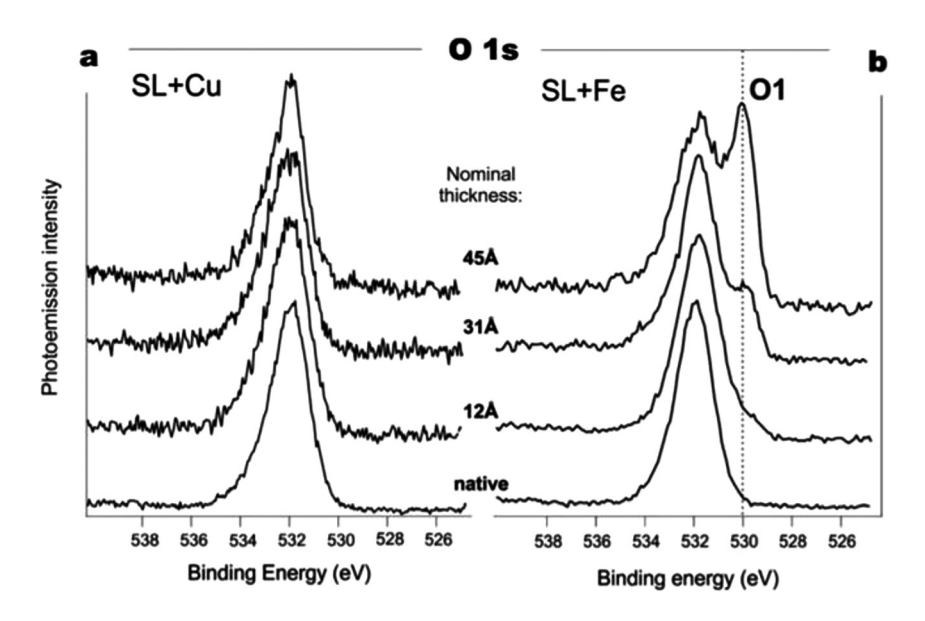
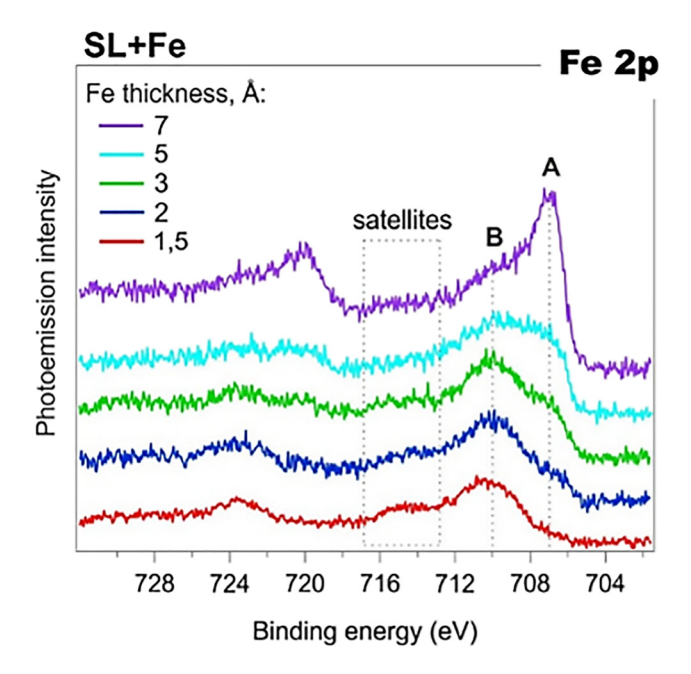


Figure 25: N 1s core-level spectra for native surface layer proteins and after the deposition of a) copper and b) iron with varying nominal thickness [80].



**Figure 26:** O 1s core-level spectra for native surface layer proteins and after the deposition of a) copper and b) iron with varying nominal thickness [80].



**Figure 27:** Fe 2*p* core-level spectra with varying deposition of Fe on SL [80].

This XPS study helped in understanding the binding mechanism involved in the cadmium, lead, and nickel biosorption process in S. vulgaris [85]. In the case of cadmium, the Cd<sup>2+</sup> cations bind with the carbon and oxygen groups present in carboxylic groups, with nitrogen present in the amino acids and sulfur present in the thiol groups of polysaccharides and amino acids. Chelation is the process by which the action of chelating agents removes specific toxic metals. Chelating agents are the inorganic and organic compounds bound with the metal ions to form a complex structure that is eventually excreted out of the biological system through extracellular or intracellular spaces [86]. However, smaller changes in the concentration of calcium and magnesium indicates that the major binding mechanism might not be ion exchange. In the case of lead, the trend was similar to the Cd<sup>2+</sup> uptake except that the magnesium and calcium concentrations decreased significantly suggesting the sequestration mechanism for lead cation was chelation, reduction, and ion exchange. In the case of nickel, Ni<sup>2+</sup> cation mainly binds with oxygen-containing chemical groups which leads to the reduction in the concentrations of magnesium and calcium. This result indicates ion exchange as the most probable binding mechanism for nickel cation. The oxygen peak shift in nickel cation confirms the major role of oxygen-containing groups in the process of nickel bio adsorption. When XPS was carried out for equal molar concentrations of lead and nickel on Sargassum samples, the concentration of lead was 10 times larger than the concentration of nickel. This result indicates the higher affinity of lead towards the biomass and its ability to form covalent or coordinative bonds with the ligands. In the case of nickel, it mainly has ionic interaction with ligands [85].

The studies outlined here in this review demonstrate that XPS can be a useful technique to study and analyze the interaction of heavy metals with DNA and some bio-metal interactions. XPS studies helped in the characterization of the changes in the chemical environments and the changes in the elemental composition before and after the bio-heavy metal interactions. XPS also complement information about the orientation and conformational changes that occur during the heavy metal ions-DNA interaction.

#### 16 Possible future directions

While studying the interaction of DNA with heavy metal ions using XPS, the X-ray beams can probe and damage the DNA itself. To study induced damage using XPS, it might be valuable to compare the soft X-ray induced radiation damage in pure DNA samples during an XPS experiment versus the accumulation of X-ray damage when metal ions coordinated with DNA. By taking XPS measurements at regular intervals, one can study the damage rate and the time evolution of the X-ray damage. The damage can lead to sample deterioration by the breaking of chemical bonds in the DNA molecules. Using the XPS spectra, the information might be obtained to indicate the change in the bonding environment over time for DNA with and without coordination with metal cations.

XPS studies of metal cation interaction with other complex biological molecules like polypeptides, both artificial as well as key proteins has not been given much attention, but like with studies of DNA, might prove valuable. There are a range of metals known to have a detrimental impact (U, Hg, Be, Os, Pb, Cd, Al) and only a few have been given attention but main group elements (Sb, As, Te, Ga, Al) and compounds and their interaction with DNA and RNA might also prove to be worthy of investigation. At present, there are not enough systematic studies to elucidate how similar metals or compounds might differ in their interaction with important chain bio molecules. For example, the effect of different actinide and lanthanide elements such as actinium, uranium, thorium etc., is not known. As a better understanding of how metals and main group elements, and their associated compounds, interact with DNA is developed, the investigation of such interactions could be expanded to be more representative of the environmental

realities. For example, naturally occurring UO<sub>2</sub> exposure could occur as a result of farming practices, and thus may be present with nitrates.

Angle-resolved photoemission studies can be performed to investigate the interaction of DNA with other heavy metals like arsenic and mercury to ascertain whether the interaction is with the surface or interior of a DNA plasmid. Taking angle resolved XPS measurements by varying the emission angles enables the detection of electrons from different depths and layers of the sample. Future studies of the interaction of DNA and RNA with metals needs to consider that both DNA and RNA are highly variable, as the DNA packaging can occur in a lot of ways. Composition and chain length are expected to matter as short chain DNA will differ from long chain DNA. The nucleobases such as adenine, guanine, thymine, cytosine, uracil can be ordered in different ways to alter the DNA/RNA sequence and the effect on binding the heavy metals has not been studied but could be. Obviously, it would be better not to depend on XPS studies alone but combine such studies with other chemistry characterization tools like electrochemical measurements such as cyclic voltammetry (CV) and other spectroscopic techniques that do not require a vacuum, such as infrared absorption and Raman. Both of the latter techniques have already been widely used to study biomolecules and cells as Raman is emerging as a possible foundational tool in chemical and biohazard sensing.

**Author contributions:** All the authors have accepted responsibility for the entire content of this submitted manuscript and approved submission.

**Research funding:** This work was supported by Science and Engineering Research Board and National Science Foundation (NSF-DMR: 1827690 and 2003057).

**Conflict of interest statement:** The authors declare no conflicts of interest regarding this article.

#### References

- 1. Jaishankar M., Tseten T., Anbalagan N., Mathew B. B., Beeregowda K. N. Toxicity, mechanism and health effects of some heavy metals. *Interdiscipl. Toxicol.* 2014, 7, 60–72.
- 2. Squibb K. S., Fowler B. A. Relationship between metal toxicity to subcellular systems and the carcinogenic response. *Environ. Health Perspect.* 1981, 40, 181–188.
- Alkorta I., Hernández-Allica J., Becerril J. M., Amezaga I., Albizu I., Garbisu C. Recent findings on the phytoremediation of soils contaminated with environmentally toxic heavy metals and metalloids such as zinc, cadmium, lead, and arsenic. Rev. Environ. Sci. Biotechnol. 2004, 3, 71–90
- Schützendübel A., Polle A. Plant responses to abiotic stresses: heavy metal-induced oxidative stress and protection by mycorrhization. J. Exp. Bot. 2002, 53, 1351–1365.
- 5. Anastassopoulou J. Metal-DNA interactions. J. Mol. Struct. 2003, 651–653, 19–26.

- 6. Breaker R. R., Joyce G. F. A DNA enzyme that cleaves RNA. Chem. Biol. 1994, 1, 223-229.
- 7. Lu Y., Liu J., Li J., Bruesehoff P. J., Pavot C. M. B., Brown A. K. New highly sensitive and selective catalytic DNA biosensors for metal ions. *Biosens. Bioelectron.* 2003, *18*, 529–540.
- 8. Brown A. K., Liu J., He Y., Lu Y. Biochemical characterization of a uranyl ion-specific DNAzyme. *ChemBioChem* 2009, *10*, 486–492.
- 9. Liu J., Brown A. K., Meng X., Cropek D. M., Istok J. D., Watson D. B., Lu Y. A catalytic beacon sensor for uranium with parts-per-trillion sensitivity and millionfold selectivity. *Proc. Natl. Acad. Sci. U. S. A.* 2007, *104*, 2056–2061.
- Lan T., Furuya K., Lu Y. A highly selective lead sensor based on a classic lead DNAzyme. Chem. Commun. 2010, 46, 3896–3898.
- 11. Barlow S. M., Raval R. Complex organic molecules at metal surfaces: bonding, organisation and chirality. *Surf. Sci. Rep.* 2003, *50*, 201–341.
- 12. Marti E. M., Quash A., Methivier C., Dubot P., Pradier C. M. Interaction of S-histidine, an amino acid, with copper and gold surfaces, a comparison based on RAIRS analyses. *Colloid. Surface. Physicochem. Eng. Aspect.* 2004, *249*, 85–89.
- 13. Vallee A., Humblot V., Pradier C. M. Peptide interactions with metal and oxide surfaces. *Acc. Chem. Res.* 2010, *43*, 1297–1306.
- 14. Castner D. G., Ratner B. D. Biomedical surface science: foundations to frontiers. *Surf. Sci.* 2002, *500*, 28–60.
- McArthur S. L. Applications of XPS in bioengineering. Surf. Interface Anal. 2006, 38, 1380–1385.
- 16. Tománek D., Dowben P. A., Grunze M. Thermodynamic interpretation of core-level binding energies in adsorbates. *Surf. Sci.* 1983, *126*, 112–119.
- 17. Egelhoff W. F. Core-level binding-energy shifts at surfaces and in solids. *Surf. Sci. Rep.* 1987, 6, 253–415.
- Jablonski A., Powell C. J. Relationships between electron inelastic mean free paths, effective attenuation lengths, and mean escape depths. J. Electron. Spectrosc. Relat. Phenom. 1999, 100, 137–160.
- 19. Baer D. R., Engelhard M. H. XPS analysis of nanostructured materials and biological surfaces. J. Electron. Spectrosc. Relat. Phenom. 2010, 178–179, 415–432.
- Neal A. L., Lowe K., Daulton T. L., Jones-Meehan J., Little B. J. Oxidation state of chromium associated with cell surfaces of *Shewanella oneidensis* during chromate reduction. *Appl. Surf. Sci.* 2002, 202, 150–159.
- Ahimou F., Boonaert C. J. P., Adriaensen Y., Jacques P., Thonart P., Paquot M., Rouxhet P. G. XPS analysis of chemical functions at the surface of *Bacillus subtilis*. *J. Colloid Interface Sci*. 2007, 309, 49–55.
- Nonckreman C. J., Rouxhet P. G., Dupont-Gillain C. C. Dual radiolabeling to study protein adsorption competition in relation with hemocompatibility. J. Biomed. Mater. Res. 2006, 79, 963–973.
- 23. Hanawa T., Hiromoto S., Yamamoto A., Kuroda D., Asami K. XPS characterization of the surface oxide film of 316L stainless steel samples that were located in quasi-biological environments. *Mater. Trans.* 2002, *43*, 3088–3092.
- 24. Murgunde B. K., Rabinal M. K., Kalasad M. N. Biologically active nanocomposite of DNA-PbS nanoparticles: a new material for non-volatile memory devices. *Appl. Surf. Sci.* 2018, 427, 344–353
- 25. Jayakumar K., Camarada M. B., Dharuman V., Rajesh R., Venkatesan R., Ju H., Maniraj M., Rai A., Barman S. R., Wen Y. Layer-by-layer-assembled AuNPs-decorated first-generation

- poly(amidoamine) dendrimer with reduced graphene oxide core as highly sensitive biosensing platform with controllable 3D nanoarchitecture for rapid voltammetric analysis of ultratrace DNA hybridiza. *ACS Appl. Mater. Interfaces* 2018, *10*, 21541–21555.
- 26. Yu K., Wei T., Li J., Wang Z., Dai Z. Construction of molecular sensing and logic systems based on site-occupying effect-modulated MOF-DNA interaction. *J. Am. Chem. Soc.* 2020, *142*, 21267–21271.
- 27. Furukawa M., Yamada T., Katano S., Kawai M., Ogasawara H., Nilsson A. Geometrical characterization of adenine and guanine on Cu(110) by NEXAFS, XPS, and DFT calculation. *Surf. Sci.* 2007, *601*, 5433–5440.
- Acres R. G., Cheng X., Beranová K., Bercha S., Skála T., Matolín V., Xu Y., Prince K. C., Tsud N. An experimental and theoretical study of adenine adsorption on Au(111). *Phys. Chem. Chem. Phys.* 2018, 20, 4688–4698.
- Bercha S., Bhasker-Ranganath S., Zheng X., Beranová K., Vorokhta M., Acres R. G., Skála T., Matolín V., Prince K. C., Xu Y., Tsud N. Adsorption structure of adenine on cerium oxide. *Appl. Surf. Sci.* 2020, *530*, 147257.
- 30. Tsud N., Bercha S., Ševčíková K., Acres R. G., Prince K. C., Matolín V. Adenine adlayers on Cu(111): XPS and NEXAFS study. *J. Chem. Phys.* 2015, 143, 174704.
- 31. Seifert S., Gavrila G. N., Zahn D. R. T., Braun W. The molecular orientation of DNA bases on H-passivated Si(1 1 1) surfaces investigated by means of near edge X-ray absorption fine structure spectroscopy. *Surf. Sci.* 2007, *601*, 2291–2296.
- Plekan O., Feyer V., Richter R., Coreno M., de Simone M., Prince K. C., Trofimov A. B., Gromov E. V., Zaytseva I. L., Schirmer J. A theoretical and experimental study of the near edge X-ray absorption fine structure (NEXAFS) and X-ray photoelectron spectra (XPS) of nucleobases: thymine and adenine. *Chem. Phys.* 2008, 347, 360–375.
- 33. Feyer V., Plekan O., Prince K. C., Šutara F., Skála T., Cháb V., Matolín V., Stenuit G., Umari P. Bonding at the organic/metal interface: adenine to Cu(110). *Phys. Rev. B* 2009, *79*, 155432.
- 34. Tsud N., Acres R. G., Iakhnenko M., Mazur D., Prince K. C., Matolín V. Bonding of histidine to cerium oxide. *J. Phys. Chem. B* 2013, *117*, 9182–9193.
- 35. Chhipa H., Srinivasa Reddy T., Soni S. K., Selvakannan P. R., Bhargava S. K. Self-assembled nanostructures of phosphomolybdate, nucleobase and metal ions synthesis and their: *in vitro* cytotoxicity studies on cancer cell lines. *J. Mater. Chem. B* 2020, *8*, 11044–11054.
- 36. Mandal S., Rautaray D., Sastry M. Ag<sup>+</sup>-keggin ion colloidal particles as novel templates for the growth of silver nanoparticle assemblies. *J. Mater. Chem.* 2003, *13*, 3002–3005.
- 37. Sanyal A., Mandal S., Sastry M. Synthesis and assembly of gold nanoparticles in quasi-linear lysine-keggin-ion colloidal particles. *Adv. Funct. Mater.* 2005, *15*, 273–280.
- 38. Ma N., Ren X., Wang H., Kuang X., Fan D., Wu D., Wei Q. Ultrasensitive controlled release aptasensor using thymine-Hg<sup>2+</sup>-thymine mismatch as a molecular switch for Hg<sup>2+</sup> detection. *Anal. Chem.* 2020, *92*, 14069–14075.
- 39. Yuan H., Sun G., Peng W., Ji W., Chu S., Liu Q., Liang Y. Thymine-functionalized gold nanoparticles (Au NPs) for a highly sensitive fiber-optic surface plasmon resonance mercury ion nanosensor. *Nanomaterials* 2021, *11*, 397.
- 40. Howorka S. DNA nanoarchitectonics: assembled DNA at interfaces. *Langmuir* 2013, *29*, 7344–7353.
- 41. Fu J., Liu M., Liu Y., Yan H. Spatially-interactive biomolecular networks organized by nucleic acid nanostructures. *Acc. Chem. Res.* 2012, *45*, 1215–1226.

- 42. Volkov I. L., Smirnova A., Makarova A. A., Reveguk Z. V., Ramazanov R. R., Usachov D. Y., Adamchuk V. K., Kononov A. I. DNA with ionic, atomic, and clustered silver: an XPS study. *J. Phys. Chem. B* 2017, *121*, 2400–2406.
- 43. Majumder S., Priyadarshini M., Subudhi U., Chainy G. B. N., Varma S. X-ray photoelectron spectroscopic investigations of modifications in plasmid DNA after interaction with Hg nanoparticles. *Appl. Surf. Sci.* 2009, *256*, 438–442.
- 44. Birnboim H. C. A. Rapid alkaline extraction method for the isolation of plasmid DNA. *Methods Enzymol.* 1983, 100, 243–255.
- 45. Burda J. V., Šponer J., Leszczynski J., Hobza P. Interaction of DNA base pairs with various metal cations (Mg<sup>2+</sup>, Ca<sup>2+</sup>, Sr<sup>2+</sup>, Ba<sup>2+</sup>, Cu<sup>+</sup>, Ag<sup>+</sup>, Au<sup>+</sup>, Zn<sup>2+</sup>, Cd<sup>2+</sup>, and Hg<sup>2+</sup>): nonempirical *ab initio* calculations on structures, energies, and nonadditivity of the interaction. *J. Phys. Chem. B* 1997, 101, 9670–9677.
- 46. Fraker A. C., Ruff A. W., Sung P., Van Orden A. C., Speck K. M. *Surface Preparation and Corrosion Behavior of Titanium Alloys for Surgical Implants*; ASTM Spec. Tech. Publ.: Philadelphia, USA, 1983; pp. 206–219.
- 47. Majumder S., Mishra I., Subudhi U., Varma S. Enhanced biocompatibility for plasmid DNA on patterned TiO<sub>2</sub> surfaces. *Appl. Phys. Lett.* 2013, *103*, 063103.
- 48. Gong Y., Misture S. T., Gao P., Mellott N. P. Surface roughness measurements using power spectrum density analysis with enhanced spatial correlation length. *J. Phys. Chem. C* 2016, 120, 22358–22364.
- Caló A., Stoliar P., Bystrenova E., Valle F., Biscarini F. Measurement of DNA morphological parameters at highly entangled regime on surfaces. J. Phys. Chem. B 2009, 113, 4987–4990.
- Ono A., Cao S., Togashi H., Tashiro M., Fujimoto T., MacHinami T., Oda S., Miyake Y.,
  Okamoto I., Tanaka Y. Specific interactions between silver(I) ions and cytosine-cytosine pairs in DNA duplexes. *Chem. Commun.* 2008, 4825–4827; https://doi.org/10.1039/b808686a.
- Swasey S. M., Leal L. E., Lopez-Acevedo O., Pavlovich J., Gwinn E. G. Silver (I) as DNA glue: Ag<sup>+</sup>-mediated guanine pairing revealed by removing Watson-Crick constraints. Sci. Rep. 2015, 5, 1–9.
- 52. Zinchenko A. A., Yoshikawa K., Baigl D. DNA-templated silver nanorings. *Adv. Mater.* 2005, *17*, 2820–2823.
- 53. Wang Y., Ran S., Man B., Yang G. DNA condensations on mica surfaces induced collaboratively by alcohol and hexammine cobalt. *Colloids Surf. B Biointerfaces* 2011, *83*, 61–68.
- 54. Gosule L. C., Schellman J. A. DNA condensation with polyamines. I. Spectroscopic studies. *J. Mol. Biol.* 1978, *12*1, 311–326.
- 55. Kral T., Hof M., Langner M. The effect of spermine on plasmid condensation and dye release observed by fluorescence correlation spectroscopy. *Biol. Chem.* 2002, *383*, 331–335.
- Qin C., Kang F., Zhang W., Shou W., Hu X., Gao Y. Environmentally-relevant concentrations of Al(III) and Fe(III) cations induce aggregation of free DNA by complexation with phosphate group. Water Res. 2017, 123, 58–66.
- 57. Asanuma H., Noguchi H., Uosaki K., Yu H. Z. Metal cation-induced deformation of DNA self-assembled monolayers on silicon: vibrational sum frequency generation spectroscopy. *J. Am. Chem. Soc.* 2008, *130*, 8016–8022.
- 58. Lee C. Y., Gong P., Harbers G. M., Grainger D. W., Castner D. G., Gamble L. J. Surface coverage and structure of mixed DNA/alkylthiol monolayers on gold: characterization by XPS, NEXAFS, and fluorescence intensity measurements. *Anal. Chem.* 2006, *78*, 3316–3325.

- 59. Petrovykh D. Y., Kimura-Suda H., Tarlov M. J., Whitman L. J. Quantitative characterization of DNA films by X-ray photoelectron spectroscopy. *Lanamuir* 2004, *20*, 429–440.
- 60. Saprigin A. V., Thomas C. W., Dulcey C. S., Patterson C. H., Spector M. S. Spectroscopic quantification of covalently immobilized oligonucleotides. *Surf. Interface Anal.* 2005, *37*, 24–32.
- 61. Voicu R., Boukherroub R., Bartzoka V., Ward T., Wojtyk J. T. C., Wayner D. D. M. Formation, characterization, and chemistry of undecanoic acid-terminated silicon surfaces: patterning and immobilization of DNA. *Langmuir* 2004, *20*, 11713–11720.
- 62. Dhiman N., Bonilla R., O'Kane J. D., Poland G. A. Gene expression microarrays: a 21st century tool for directed vaccine design. *Vaccine* 2001, *20*, 22–30.
- 63. Liu Q., Wang L., Frutos A. G., Condon A. E., Corn R. M., Smith L. M. DNA computing on surfaces. *Nature* 2000, *403*, 175–179.
- 64. Jackson N. M., Hill M. G. Electrochemistry at DNA-modified surfaces: new probes for charge transport through the double helix. *Curr. Opin. Chem. Biol.* 2001, *5*, 209–215.
- 65. Liu S. Q., Xu J. J., Chen H. Y. A reversible adsorption-desorption interface of DNA based on nano-sized zirconia and its application. *Colloids Surf. B Biointerfaces* 2004, *36*, 155–159.
- 66. Rinaudo M. Chitin and chitosan: properties and applications. *Prog. Polym. Sci.* 2006, *31*, 603–632.
- 67. Shahidi F., Arachchi J. K. V., Jeon Y. J. Food applications of chitin and chitosans. *Trends Food Sci. Technol.* 1999, *10*, 37–51.
- 68. Liu S., Kang M., Yan F., Peng D., Yang Y., He L., Wang M., Fang S., Zhang Z. Electrochemical DNA biosensor based on microspheres of cuprous oxide and nano-chitosan for Hg(II) detection. *Electrochim. Acta* 2015, *160*, 64–73.
- 69. Zhang X., Wang G., Gu A., Wu H., Fang B. Preparation of porous Cu<sub>2</sub>O octahedron and its application as L-tyrosine sensors. *Solid State Commun.* 2008, 148, 525−528.
- Zhang X., Wang G., Zhang W., Wei Y., Fang B. Fixure-reduce method for the synthesis of Cu<sub>2</sub>O/MWCNTs nanocomposites and its application as enzyme-free glucose sensor. *Biosens. Bioelectron.* 2009, 24, 3395–3398.
- 71. Fan H. T., Teng X. M., Pan S. S., Ye C., Li G. H., Zhang L. D. Optical properties of δ-Bi<sub>2</sub>O<sub>3</sub> thin films grown by reactive sputtering. *Appl. Phys. Lett.* 2005, *87*, 231916.
- 72. Kim H. W., Lee J. W., Shim S. H., Kebede M. A., Lee C. Crystalline bismuth oxide nanorods fabricated on Pt-coated substrates using a trimethylbismuth and oxygen mixture. *Cryst. Res. Technol.* 2008, 43, 695–699.
- 73. Duan X., Huang Y., Cui Y., Wang J., Lieber C. M. Indium phosphide nanowires as building blocks for nanoscale electronic and optoelectronic devices. *Nature* 2001, *409*, 66–69.
- 74. Hale M. G., Little R., Salem M. A., Hedley J. H., Horrocks B. R., Šiller L. Formation of bismuth oxide nanowires by simultaneous templating and electrochemical adhesion of DNA on Si/SiO<sub>2</sub>. *Thin Solid Films* 2012, *520*, 7044–7048.
- 75. Taniguchi M., Kawai T. DNA electronics. *Phys. E Low-Dimens. Syst. Nanostruct.* 2006, *33*, 1–12.
- Zhang Z., Gekhtman D., Dresselhaus M. S., Ying J. Y. Processing and characterization of single-crystalline ultrafine bismuth nanowires. *Chem. Mater.* 1999, 11, 1659–1665.
- 77. Wingender J., Neu T. R., Flemming H. C. What are bacterial extracellular polymeric substances?; *Microb. Extracell. Polym. Subst.*; Springer: Berlin, Heidelberg, 1999; pp. 1–19.
- 78. Steinberger R. E., Holden P. A. Extracellular DNA in single- and multiple-species unsaturated biofilms. *Appl. Environ. Microbiol.* 2005, *71*, 5404–5410.

- 79. Hufton J., Harding J. H., Romero-González M. E. The role of extracellular DNA in uranium precipitation and biomineralisation. *Phys. Chem. Chem. Phys.* 2016, *18*, 29101–29112.
- Makarova A. A., Grachova E. V., Neudachina V. S., Yashina L. V., Blüher A., Molodtsov S. L., Mertig M., Ehrlich H., Adamchuk V. K., Laubschat C., Vyalikh D. V. Insight into bio-metal interface formation in vacuo: interplay of S-layer protein with copper and iron. *Sci. Rep.* 2015, 5, 1–7.
- 81. Schedel-Niedrig T., Weiss W., Schlögl R. Electronic structure of ultrathin ordered iron oxide films grown onto Pt (111). *Phys. Rev. B* 1995, *52*, 17449.
- 82. Graat P. C., Somers M. A. Simultaneous determination of composition and thickness of thin iron-oxide films from XPS Fe 2p spectra. *Appl. Surf. Sci.* 1996, 100–101, 36–40.
- 83. Schiewer S., Volesky B. Modeling multi-metal ion exchange in biosorption. *Environ. Sci. Technol.* 1996, *30*, 2921–2927.
- 84. Krishnani K. K., Meng X., Christodoulatos C., Boddu V. M. Biosorption mechanism of nine different heavy metals onto biomatrix from rice husk. *J. Hazard. Mater.* 2008, *153*, 1222–1234.
- 85. Raize O., Argaman Y., Yannai S. Mechanisms of biosorption of different heavy metals by brown marine macroalgae. *Biotechnol. Bioeng.* 2004, *87*, 451–458.
- 86. Flora S. J. S., Pachauri V. Chelation in metal intoxication. *Int. J. Environ. Res. Publ. Health* 2010, 7, 2745–2788.